Investigations on dye adsorption and photocatalytic Cr-(VI) reduction by SnS_2 nanosheets prepared via hydrothermal method

Sandita Das

MS15193

A Dissertation submitted for the partial fulfillment of BS-MS Dual Degree in Science.

Department of Chemical Sciences
Indian Institute of Science Education and Research Mohali
India
June 2020.

Certificate of Examination

This is to certify that the dissertation titled **"Investigations on dye adsorption and photocatalytic Cr-(VI) reduction by SnS_2 nanosheets prepared via hydrothermal method"** submitted by **Ms. Sandita Das** (Reg. No. MS15193) for the fulfillment of **BS-MS dual degree programme** of the Institute, has been examined by the thesis committee duly appointed by the Institute. The committee finds the work done by the candidate satisfactory and recommends that the report be accepted.

Dr. Angshuman Roy Choudhury Dr. Debrina Jana Dr. Ujjal K. Gautam

(Supervisor)

Dated 15/06/2020

Declaration

The work presented in the dissertation has been carried out by me under the guidance of Dr. Ujjal K. Gautam at the Indian Institute of Science Education and Research, Mohali.

This work has not been submitted in part or in full for a degree, a diploma or a fellowship to any university or institute. Whenever contributions of others are involved, every effort is made to indicate this clearly, with due acknowledgment of collaborative research and discussions. This thesis is a bonafide record of original work done by me and all sources listed withing have been detailed in the bibliography.

Sandita Das
(Candidate)
June 15, 2020

In my capacity as the supervisor of the candidate's project work, I certify that the above statements by the candidate are true to the best of my knowledge.

Dr. Ujjal K. Gautam
(Supervisor)

Acknowledgements

Foremost, I would like to express my profound gratitude to my parents and my elder brother for their continuous support, words of encouragement and wisdom. I owe it to them, whatever I have managed to achieve in my life.

I am very grateful to my thesis advisor Dr. Ujjal K Gautam for his expert supervision. He pushed me out of my comfort zone and made me realize my potential. He takes the time and effort to individually guide his students, which was pivotal to the completion of this thesis.

I would like to extend my thanks to all my lab members. Sanjit and Maqsuma guided me throughout my time in the lab and trained me to work independently. Sanjit along with Kaustav, introduced me to the field, taught me how to approach the problem, form hypotheses and analyze and document results, and I am very grateful for that. I am thankful to Lipipuspa, Raj, Reeya, Komal and Parmeet for making the lab environment fun and efficient.

Last but not least, I would like to extend my thanks to my dear friends Shweta, Sudha, Arghadip, Tisya and, Pinku who helped me sail through the last five years.

Contents

List of figures

List of tables

Notation

ºC- Centigrade

DRS- Diffuse Reflectance Spectroscopy.

PXRD- Powder X-ray Diffraction.

TEM- Transmission Electron Microscopy.

HRTEM- High Resolution Transmission Electron Microscopy.

SAED- Selected Area Electron Diffraction.

EDS- Energy-dispersive X-ray Spectroscopy.

BET- Brunauer-Emmett-Teller.

RhB- Rhodamine B.

MB- Methylene Blue.

UV-Vis – UV-Visible Spectroscopy.

μM- Micromolar.

rpm- Revolutions per minute.

mL- Millilitre.

nm- Nanometre.

mg- milligram

mins- minutes

hrs- hours

NSs- nanosheets

NTs- nanotubes

NWs-nanowires

NPs- nanoparticles

AC- activated carbon

GO- Graphene oxide

RGO- reduced graphene oxide.

AO- ammonium oxalate

MO- Methyl orange.

ABSTRACT

In recent years, metal chalcogenide photocatalysts with high performance for water treatment and pollutant degradation under visible-light have attracted considerable interest in solving energy and environmental issues. Metal chalcogenide semiconductors have found applications in various fields of science as well such as solar cells, sensors, polarizers, and thermoelectric cooling materials. In this thesis, we have synthesized tin sulfide (SnS_2) nanosheets, a metal chalcogenide with the crystalline structure CdI_2 comprised of triple plane layers of S-Sn-S by strong ion-covalent bonds coupled with weak Van der Waals forces, using conventional hydrothermal method. The prepared catalyst was characterized by PXRD, TEM, HRTEM, DRS, and BET which inferred they were nanometer in size with a bandgap in the visible range.

The as-synthesized SnS_2 nanosheets were used for adsorption of organic dyes- RhB, methylene blue, and methyl orange. It is observed that the catalyst has more adsorption capacity for RhB than that of methylene blue. We also found the effect of different pH on adsorption and it has been observed that the adsorption process is much more facilitated in the basic medium in case of methylene blue; however, in the case of RhB, the adsorption process is not regular at pH>10. The prepared SnS_2 catalyst has shown 90% adsorption of methylene blue up to 5 cycles. Both the adsorption process followed pseudo-second-order kinetics and Langmuir adsorption isotherm implying adsorption due to chemisorption and monolayer adsorption. The prepared SnS_2 NSs did not show any adsorption of methyl orange which indicates that the adsorbent has (-)ve surface charge and it capable of adsorbing cationic dyes.

Photocatalytic reduction of Cr-(VI) is also carried out using the as-synthesized SnS_2 nanosheets. It has been observed that the catalyst is capable of 95% removal of Cr-(VI) in 26 minutes in the presence of ammonium oxalate, a hole scavenger, in Xenon lamp. The reaction follows pseudo-first-order kinetics with a rate constant of 0.1 min^{-1}.

This study suggests that as-prepared SnS_2 nanosheets can be considered as a promising catalyst for wastewater purification and pollutant degradation.

1. INTRODUCTION

The discharge of industrial waste in water bodies poses an enormous danger to human health and the environment. Pollution by wastewater effluents containing synthetic dyes has been a potential hazard for our environment, and it disturbs the whole food web and thus affecting all living beings. The dye industries comprise a small part of the overall chemical industries. Dyes have been used extensively for many years for textile, paints, pigments, printing, rubber, cosmetics, leather, and other applications[1 2 3 4]. Today, textile industries manufacture at least 100,000 different types of dyes. To meet industrial demands, about 1.6 million tons of dyes are produced annually, of which 10-15% goes off to watercourses as wastewater during the different process of textile industries making dyes as one of the toxic pollutants.[1] Dyes are chemical compounds that impart colors by attaching to fabrics. Getting rid of dyes from textile and other industries is a significant challenge for the environment as they are water-soluble and yield bright colors in water with acidic properties[2]. Many health problems arise due to excessive exposure to dyes. The most common health hazard is respiratory problems due to inhalation of dye particles which leads to respiratory sensitization with symptoms such as itching, watery eyes, sneezing, coughing and wheezing. Some reactive, disperse dyes are classified as skin sensitive such as formaldehyde-based resins, ammonia, acetic acid, shrink-resist chemicals causing skin irritation, sore eyes and blocked nose[4]. A vast amount of dye discharges in water bodies causes high chemical oxidation demand resulting in foul odor thus hampering the aquatic life[1]. Therefore, it is essential to remove dyes from wastewater effectively to ensure the safe discharge of liquid effluents in water bodies.

There are several physicochemical and biological ways of treating wastewater. The physical methods for dye removal are adsorption, ion exchange, and filtration/coagulation, etc. while chemical processes include ozonization, Fenton's reaction, photocatalytic reaction, and biological processes include aerobic degradation, anaerobic degradation and biosorption etc.[2] The selection of the technique of dye removal depends on the properties of the wastewater. Each method has its limitation in terms of cost-effectiveness, feasibility, reliability, sludge formation, the release of byproducts[5]. Below mentioned are some of the means of dye removal with their constraints[5].

- Chemical precipitation- Consumption of oxidants and formation of sludge, which leads to disposal problems.
- Coagulation/Flocculation- Requires adjunction of re-usable chemicals like coagulants, flocculants, and aid chemicals. It produces an increased volume of sludge generation, which is difficult to handle.
- Froth Floatation- Not cost-effective as it needs enormous energy, investment, and maintenance, and selectivity is pH-dependent.
- Chemical oxidation- Involves the usage of oxidants that are toxic and generates sludge.
- Ion exchange- It does not apply to all types of dyes. It is not a cost-effective procedure.
- Membrane filtration- Limited flow rates. The choice of membranes depends upon the application. It requires enormous investment and maintenance costs.

Adsorption is one of the practical and accessible methods for dye removal. Adsorption is a surface phenomenon where the adsorbable solute, called the adsorbate, interacts with the adsorbent molecule, with a highly porous surface, due to intermolecular attraction resulting in the concentration molecule on the solid adsorbent surface[2]. Most of the industries demand fast removal of contaminants efficiently for which research on nanomaterial adsorbent came to exist. Nanomaterials are a significant candidate for adsorption due to their high surface area, thus providing more active sites. They are easily synthesized and a small amount is required for the effective removal of pollutants[1]. Some of the nanomaterial adsorbents known to remove heavy metals are ZnO, CeO_2, etc[1]. Dyes can be categorized into ionic and non-ionic. Vat dyes and disperse dyes fall into non-ionic dyes, and cationic and anionic dyes fall into the ionic dyes category[1].

Activated carbon is an essential adsorbent for dyes removal[3] [1], but it is quite expensive because of its production coat. Carbon nanotubes and their composites are known to be useful adsorbents[1]. Another carbonaceous material is nanodiamond that can adsorb dyes[1]. The most common and popularly used semiconductor material is TiO_2. Several synthetic procedures are used to prepare TiO_2 of different morphologies like nano TiO_2, TiO_2 nanotubes[1], etc. to increase their adsorbing performance. Magnetic nanomaterials are also

being used for adsorbents purpose to make the whole process more economical. Some of the magnetic nanoparticles known are Fe_3O_4 nanoparticles and ilmenite $FeTiO_3$ nanoparticles known for adsorption of Rhodamine B and methylene blue dyes[1]. While searching for cheap and low-cost adsorbents, researchers have derived adsorbents from natural materials such as spent coffee grounds[6], peels of fruits like orange and banana[7]. Some other bio-adsorbents for methylene blue are kaolinite[8], neem leaf powder[9], wheat shells[10], dehydrated peanut shells[11], rice husks[6], cereal chaff[12] etc. However, the adsorption capacities of these bio-adsorbents are less, and they cannot be applied on an industrial scale where a massive amount of dye has to be adsorbed in a short time[1]. Graphene, graphene oxide[13], and their composites like GO/calcium alginates[14], GNS-Fe_3O_4 NPs[15] proved to be promising candidates for adsorption of dyes. Several natural zeolites[16], metal sulfides[17 18], and oxides[1] have also been designed for this purpose. Some reported metal oxides and their composites are TiO_2,[1] ZnO NPs[1], FeO[19], WO_3 NRs[20], Co_3O_4 NPs[21], $W_{18}O_{49}$ NWs[22], magnetic AC/CeO_2,[23] for adsorption of organic dyes. SnS_2 and MoS_2 composites such as SnS_2/rGO[24], SnS_2/MoS_2,[17] magnetic Fe_3O_4/MoS_2 [25]are also known for organic dye adsorption. Various morphologies of MoS_2 have been prepared like nanosheets[18], sponges[26] for enhancing the adsorption activity. SnS_2 is also a popular adsorbent and many micro and nanostructures have been synthesized for dye removal and degradation in previous research articles[24 27 28 29].

Photocatalytic Cr (VI) reduction

Exposure to heavy metals is also a severe threat to human health. Many industrial activities such as leather tanning, steel production, electroplating, textile industries, paints, and pigments, fertilizing, photographic, etc. lead to Cr (VI) discharge[30 31 32 33]. Hexavalent chromium (Cr (VI)) is known to be the second most inorganic pollutant after lead (Pb)[34]. Cr-(VI) is considered toxic when its concentration is above 0.05mg/L[30] and causes damage and irritation to human skin[31]. It has been categorized as a group I human carcinogen by the International Agency for Research on Cancer, considering its toxicities[31]. Cr (VI) is carcinogenic due to its ability to generate reactive oxygen species in cells causing liver damage, pulmonary congestion, severe vomiting and diarrhea[35] and it has high migration to water thus contaminating ground and surface water[32 36]. On the contrary, Cr (III) is a useful nutrient for living beings[31 34]. Therefore, it is necessary to convert toxic Cr (VI) to useful Cr

(III) for the remediation of environmental pollution caused by Cr-(VI)[33]. There are many conventional processing techniques for this purpose such as ion exchange, chemical precipitation, membrane filtration, biological, chemical and electrochemical reduction and adsorption[37]. All these methods are not cost-effective and show less removal of Cr-(VI). There are certain limitations to these techniques such as the Cr (III) released into the environment that can again oxidize to Cr-(VI) pollute the surface water and also use of high energy or extensive use of reducing agents. To solve these problems, there are specific techniques to be used which are labor-extensive[38]. Therefore, it is essential to design a method that is effective, environmental-friendly and economical for the reduction of Cr (VI). Semiconductor mediated photocatalytic Cr (VI) reduction is one of the efficient, sustainable, clean and cost-effective techniques that are used nowadays. This process involves the direct use of infinite sunlight, recyclability and there is no release of unwanted chemicals under ambient conditions[30 36].

So far, there are many reports on photocatalysts for the reduction of Cr (VI), TiO_2 being the most common photocatalyst. TiO_2 and its different composites have been synthesized over the years and have been utilized for Cr (VI) reduction. Generally, the problem of small bandgap and recombination of photogenerated holes and electrons arise. The solution to this problem lies in the coupling of a semiconductor with the catalyst, which adjusts the bandgap to our required value and also enhances the activity. TiO_2 has also been coupled with SnS_2[39], Au[40], ZnO[31], reduced graphene oxide[37] and carbon which gave good activity. CdS is also a popular photocatalyst used in photocatalytic reduction of Cr (VI). $CuFe_2O_4$/CdS[41], CdS/α-Fe_2O_3 heterojunction nanocomposite[30], CdS/SnO_2[42], $ZnFe_2O_4$/CdS nanorods[43] had been known to be reported with highly efficient reduction of Cr (VI). Since CdS is toxic, therefore alternatives are being designed as well. Metal-Organic Frameworks (MOF) had also been utilized for this same purpose. MOFs, incorporated with $–NH_2$ groups, photocatalysts like ZnO, metal sulfide compounds such as SnS[44], novel nanoparticles like Pd nanoparticles[34] and graphene oxide, showed better performance for Cr (VI) reduction[32]. Quantum dots have also been used for Cr (VI) reduction and its composites as well[45]. Some other photocatalysts reported are CuS nanostructures[46], CoO nanoparticles[47], $ZnWO_4$ nanostructures[48], Mg-doped WO_3[49], In-doped compounds[50], SnO_2/SnS_2[51] nanocomposite which have shown an efficient reduction of Cr (VI).

Photocatalysis

Catalyst is a component that enhances the rate of the reaction without changing the total Gibbs energy in the reaction and it is restored after every catalytic activity. It doesn't influence the thermodynamic equilibrium composition after the end of the reaction. Photocatalysis is the action happening when light interacts with the semiconductor material called the photocatalyst and leads to the chemical transformation of the reactant participants. During this process, light falls on the semiconductor photocatalyst leading to holes and electrons formation in the valence band and conduction band, respectively. Oxidation from photogenerated holes and reduction from photogenerated electrons happen simultaneously due to redox reactions. Water is converted to strong oxidizing OH- radicals in the hole, whereas electrons react with adsorbed molecular oxygen yielding superoxide radicals. Figure 1.1 gives a general outline of photocatalysis. The hydroxyl and superoxide radicals serve as powerful oxidizing agents to degrade organic dyes from wastewater.

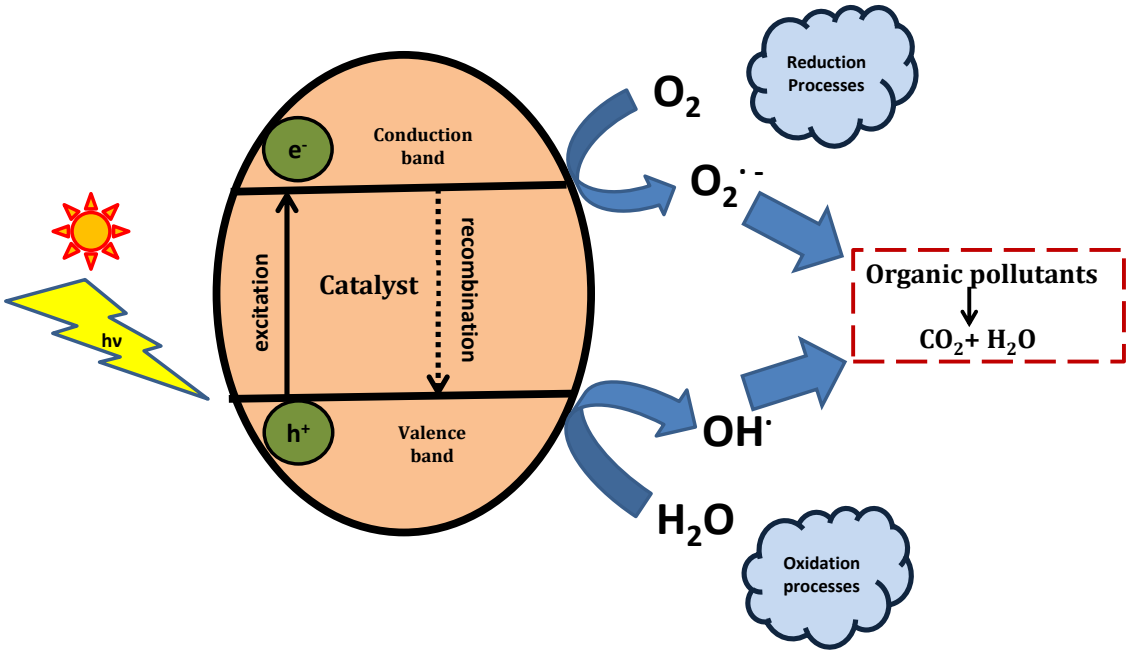

Figure 1.1 – A schematic outline of the photocatalysis reaction

Water treatment through photocatalysis has gained much attraction in the recent years. The field of photocatalysis has become much more diverse since the achievement of electrochemical photocatalysis of water on TiO_2 electrode by Fujishima and Honda in

1972[52]. Photocatalysis is an alternative for the energy-intensive conventional treatment methods utilizing renewable solar energy. This method doesn't lead to the formation of harmful byproducts and can be used for all states of pollutants[53]. Photocatalysis can be of two types- homogeneous (catalyst and reactants are in the same phase) and heterogeneous (catalyst and reactants are in different phases). Heterogeneous photocatalysis has been widely used for the treatment of organic pollutants in water and air. The benefits of heterogeneous photocatalysis over homogeneous are the catalyst can be separated after each photocatalytic cycle and thus can be reused, further making the whole process cost-effective. Semiconductor photocatalysis is a promising technique for air purification, water disinfection, and waste purification.

Metal sulfide photocatalysts

Zero dimensional metal semiconductors have gained much attention in recent years due to their physical and chemical properties. These nanostructures exhibit properties such as magnetic, optical, electronic etc which make them potential candidates for application in nanodevices[54]. Metal sulfides possess narrow band gaps making them an active class for photocatalysis besides metal oxide semiconductors[55]. Some of the well-known metal sulfides are CdS, MoS_2, SnS_2 etc. CdS has been widely used for photocatalytic purposes however, there is a requirement for its alternative due to its harmful side effects[56]. SnS_2 is an important semiconductor, which is non-toxic, synthesized in a clean and cost-effective method. SnS_2 is an *n*-type semiconductor with a bandgap of 2.18 eV-2.34 eV[55] and CdI_2-type layered hexagonal crystal structure consisting of two layers of close-packed sulfur anions with tin cations sandwiched between them in SnS_6 octahedral coordination at the edges[55]. There are several synthesis methods of SnS_2 known up to date such as hydrothermal method, microwave heating, chemical bath deposition, solid-state synthesis [55]etc. Hydrothermal synthesis is the most used technique to have the desired shape and morphology of SnS_2. According to previous literature, different morphologies of SnS_2 have been synthesized like graphene-like, nanotubes, nanosheets, nanoplates, nanocrystals, nanowires, nanobelts, spherical, nest-like, flower-like[55 57]. The narrow bandgap of SnS_2 makes it perfect for photocatalytic reactions such as water splitting[55], dye degradation[58], Cr (VI) reduction[56]. Several organic dyes such as Rhodamine B[59], methyl orange[57], methylene blue[55], phenol[60],

and heavy metals such as Pb^{2+}, Cd^{2+} are known to be adsorbed and degraded by different morphologies of SnS_2 and their composites. SnS_2 exhibits electronic properties that have been put to use in many nanodevices. SnS_2 showed excellent performance in lithium-ion batteries[61] with good cycling stability and excellent capacity retention. Despite the varied application of SnS_2, a problem of recombination of photogenerated holes and electrons is encountered. Researchers have solved this problem by coupling SnS_2 with various other semiconductors and also forming heterojunctions such as reduced graphene oxide[45], ZnS[60], SnO_2[62], and many others. All these composites show excellent performance in photocatalytic activity with good stability. SnS_2/SnO_2 composite has been known to show antimicrobial activity with the degradation of Enrofloxacin, an antibiotic pollutant[63]. SnS_2 nanoparticles have gas sensing properties[64 65]. Layers of tin sulfide crystals prepared by chemical vapor deposition have been applied in integrated nanoelectronic/photonic systems for photodetection purposes[66 67]. Different morphologies of SnS_2 are known to exhibit excellent performance for lithium-ion batteries[68 61]. The outstanding performance of SnS_2 ultrathin nanosheets on photodetectors suggested it to be a potential component for optical sensing and low power FET[69 67].

In this project, we have synthesized SnS_2 nanosheets of 25-30 nm size by hydrothermal method and studied its application on organic dye adsorption and photocatalytic Cr (VI) reduction. The synthesized SnS_2 nanosheets were characterized using XRD, BET, TEM, and HRTEM and DRS. The high porosity and surface area of as-prepared SnS_2 nanosheets proved it to be a promising component for dye removal and pollutant degradation.

2. EXPERIMENTAL SECTION

Chemicals

Tin (IV) chloride pentahydrate ($SnCl_4.5H_2O$, Sigma Aldrich. 98%), thioacetamide (Sigma Aldrich, 99.0%), absolute ethanol, Distilled Water, Methylene blue Solution (Sigma Aldrich), Rhodamine B (Sigma, >95%, HPLC), Hydrochloric Acid (HCl, Rankem), Sodium Hydroxide (NaOH, Merck), Potassium dichromate (Merck), ammonium oxalate(Merck).

Synthesis of Tin Sulphide (SnS_2) nanosheets

The synthesis of SnS_2 nanosheets has been done by a simple hydrothermal method following the given literature[70]. For the synthesis of SnS_2 nanosheets, 1mmol tin (IV) chloride pentahydrate ($SnCl_4.5H_2O$) and 4mmol thioacetamide (TAA) were mixed well in 80ml deionized water, and consequently, a transparent solution was obtained. Then the solution was transferred carefully to a 100ml Teflon-lined stainless steel autoclave and heated in an electric oven at 160^0C for 12 hours. Yellow-colored SnS_2 nanosheets were collected after washing with distilled water and ethanol followed by centrifugation in each step. Then the obtained sample was put to dry in the oven at 50^0C for 12 hours. Figure 2.1 shows the steps of synthesis, and the final compound formed.

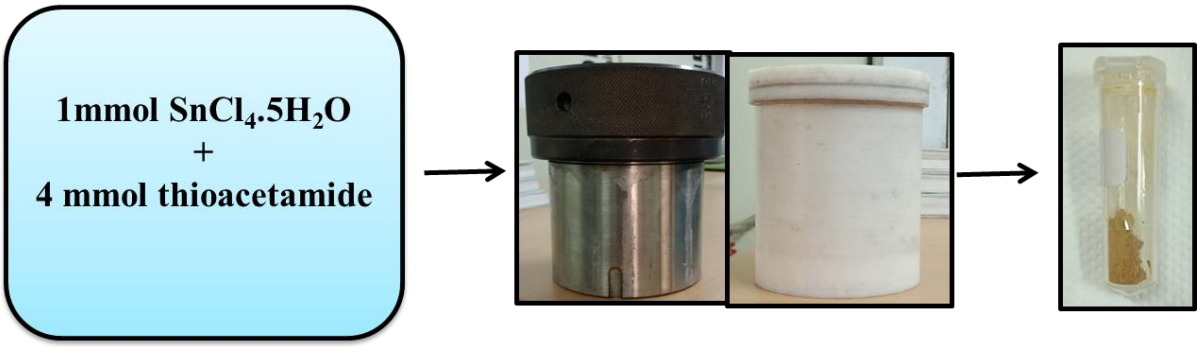

Figure 2.1- Synthesis steps and final product formed

Characterization

Powder X-ray diffraction (PXRD) pattern was collected on a Rigaku Ultima IV diffractometer equipped with a 3 kW sealed tube Cu Kα X-ray radiation (λ=1.5418 Å, 40kV and 40 mA) equipped with a DTex Ultra detector using parallel beam geometry (2.5° primary and secondary slits, 0.5° divergence slit with 10mm height limit slit). The sample, grounded into a fine powder using a mortar and a pestle, was placed on a glass sample holder for room temperature measurement. The data was collected over 2Θ from 10° to 80° with a scanning speed of 2° per minute, with a 0.01° step. The diffuse reflectance spectrum (DRS) was measured using a UV-Vis spectrophotometer (PerkinElmer, Lambda 365) and $BaSO_4$ was used as the reference. The sample was grounded into a fine powder using a mortar and pestle and then transferred carefully into the solid holder with a spatula maintain the uniformity of the sample. TEM and HRTEM were carried out using JEOL JEM-F200. TEM sample was prepared by dispersing it in ethanol and then sonicated for 10 minutes. The sample solution was then drop-casted on a holey carbon Cu-grid. The sample was dried under vacuum before starting the measurement. The BET measurements were carried out in Autosorb gas sorption analyzer (Quantachrome Instruments, Model Autosorb IQ-C-XR-XR (2 Stat.) EPDM ID 195391).

Adsorption experiments

For the adsorption experiments, methylene blue (MB) and Rhodamine B (RhB) were used. The adsorption of the aqueous solution of MB and RhB was carried out at room temperature (about 25°C). 15mg of the prepared adsorbent was added to a 50 mL aqueous solution containing a certain concentration of dye. The resulting mixture was sonicated for some seconds to ensure complete mixing of adsorbent in the solution. 3ml aliquot was collected to observe the initial absorbance by a UV-monitoring before adding the adsorbent. The sample was then poured into the solution. For MB solution, the solution was then stirred for 30 minutes and for RhB, the solution was stirred for 60 minutes in dark condition at 420 rpm on a magnetic stirrer. An aliquot of 3 mL was collected every 5 minutes to record the absorbance of the dye. The aliquot was centrifuged at 13.5 rpm for about 30 secs to 1 minute to let the adsorbent settle and then monitored by UV-Vis spectrometry (PerkinElmer,

Lambda 365). The residual concentration of the dyes (C_t) was determined by observing the change in the absorbance centered at absorption maxima. The equilibration adsorption capacity Q_e (mg g^{-1}) and adsorption capacity at time t minutes Q_t (mg g^{-1}) were calculated using the following equations:

$$Q_e = (C_0 - C_e)V/m$$

$$Q_t = (C_0 - C_t)V/m$$

Where C_0, C_e, and C_t (mg L^{-1}) are the initial, equilibrated, and t time concentrations of aqueous solutions of dyes respectively; V(L) and m(g) are the volume of solution and the amount of adsorbent respectively[59].

Kinetics of Adsorption

The applicability of pseudo-first-order and pseudo-second-order model was tested for the adsorption of RhB and MB onto prepared SnS_2 NSs. For the kinetics study, adsorption of a particular concentration of RhB and MB was carried out. The pseudo-first-order and pseudo-second-order kinetic models followed are given as:

$$\ln (Q_e - Q_t) = \ln Q_e - k_1 t$$

$$t/Q_t = 1/k_2 Q_e^2 + t/Q_e$$

where Q_e and Q_t (mg g^{-1}) are the dye adsorption capacity at equilibrium and at time t (minutes). The parameters k_1 and k_2 represented the pseudo-first-order and pseudo-second-order rate constant for the kinetic model, respectively. The parameters k_1 and Q_e for the pseudo-first-order kinetic model could be obtained from the slope and intercept of the plots of $\ln(Q_e - Q_t)$ versus t. In the case of the pseudo-second-order kinetic model, the Q_e and k_2 values can be determined from the slope and intercepts of plots of t/Q_t versus t[59 17].

Adsorption isotherms

The experimental data were fitted in both Langmuir and Freundlich Isotherms using the given equations.

Langmuir isotherm: $C_e/Q_e = C_e/Q_m + 1/k_L Q_m$

Freundlich isotherm: $\ln Q_e = \ln k_F + (1/n)\ln C_e$

where C_e is the concentration of dye at equilibrium (mg L^{-1}), Q_e is the amount of dye adsorbed by prepared SnS_2 NSs at equilibrium (mg g^{-1}), Q_m is the theoretical maximum adsorption capacity corresponding to monolayer coverage (mg g^{-1}). k_L is the Langmuir isotherm model constant (L mg^{-1}), k_F (L mg^{-1}) is the Freundlich adsorption equilibrium constant and indicates adsorption capacity, and n is a characteristic coefficient relating to adsorption intensity[59 17].

Photocatalytic activity- Cr(VI) reduction

The photocatalytic experiments were carried out in a 400 W Xe lamp as the visible light source (λ> 420 nm) with cut off filters and cooling attachments. The reactor used for the experiment is a 50 mL pyrex glass round-bottomed flask. For the Cr(VI) reduction, 25 mL of 20 ppm of $K_2Cr_2O_7$ solution, and 25 mg of catalyst(SnS_2 NSs) were used. Prior to illumination, the reaction mixture was stirred in the dark for 10 minutes for adsorption-desorption equilibrium. Ar gas was purged into the reaction mixture for 20 minutes to create an inert atmosphere with constant stirring, and the resulting reaction mixture was exposed to light for photocatalytic reduction. During the reaction, 3 mL of aliquots were collected at scheduled intervals and centrifuged for 30 minutes at 1.35 rpm to separate the photocatalyst. The Cr(VI) content in the supernatant solution was determined at~370 nm through UV-Vis spectrometry. The measured absorbance intensities at different intervals of time were transformed to the reduction of Cr(VI) following the given expression[56]-

$$\text{Reduction of Cr-(VI)} = (A_0-A_t)/A_0 \text{ X } 100\%$$

where A_0 and A_t are the absorbance intensities for initial and t minutes solutions, respectively.

3. RESULTS AND DISCUSSION

3.1 Catalyst characterization

3.1.1 Powder X-ray diffraction

Figure 3.1 shows the PXRD pattern recorded for the as-synthesized SnS_2 NSs to check the crystallinity and purity of the compound. All diffraction peaks appearing at 2θ values of 15.1, 28.5, 30.2, 32.3, 45.8, 50.1, 52.6, 58.7, 59.6, 63.1, 67.2, 70.3 correspond to the (100), (002), (101), (003), (110), (111), (200), (201), (004), (202) and (113) crystallographic planes respectively of hexagonal SnS_2 NSs respectively (ICDD# 23-0677)[55] indicating that the sample is devoid of impurities. It can be observed in the pattern that the intensities corresponding to peaks 10I (I=1, 2, 3) are low (101) or altogether missing (102), (103) suggesting poor crystallinity of this set of planes. Similar XRD patterns were observed previously also, and it appears that the 10l peak intensity depends on the synthesis conditions and becomes prominent only at high temperatures and longer reaction times[45 51 71].

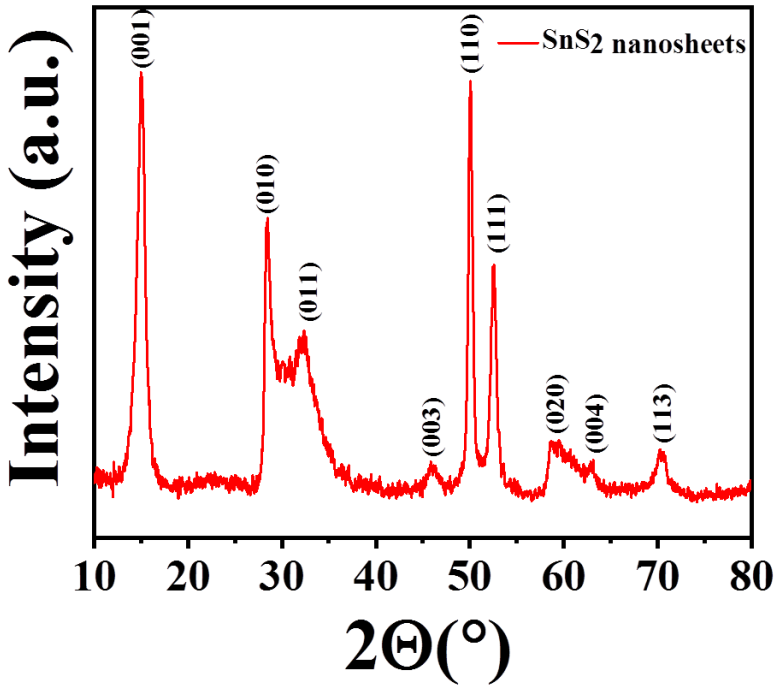

Figure 3.1 – PXRD pattern of prepared SnS_2 NSs

3.1.2 Transmission Electron Microscopy images

The morphology and size of the SnS_2 nanosheets were characterized by transmission electron microscopy (TEM). Figures 2a, b, and c show low magnification TEM images of the SnS_2 NSs. The sizes of the nanosheets are in the range of 25-30 nm. They have an approximately hexagonal shape and connected to one another. Moreover, the nanosheets tend to buckle at times forming scrolls at the edges. Figure 2d shows the TEM image of a single hexagonal nanosheet with smooth edges. A closer inspection of larger SnS_2 nanosheet shows the presence of continuous lattice fringes all across interspersed with crystal defects. Fast Fourier transformation (FFT) patterns collected from the smaller domains of the nanosheet (Figure 2e) showed that the crystal orientation is indeed identical across a nanosheet. The high resolution (HR) TEM image also shows the highly crystalline nature of the film with an inter planner distance of 0.36 nm, corresponds to the (001) plane of the hexagonal SnS_2 NS (Figure 2f). Figure 2g is the typically selected area electron diffraction (SAED) pattern acquired from a single SnS_2 NS showing the hexagonal pattern corresponding to the (001) zone axis, confirming that the sheets primarily grow in the (hk0) direction. The composition of the as-synthesized SnS_2 NSs was further analyzed by EDS measurement revealing the co-existence of Sn and S (Figure 2h) with a composition of 35.11% and 65.89% respectively, close to the ideal value. Figure 2i shows the EDS mapping of the SnS_2 NSs, showing the uniform distribution of Sn and S.

3.1.3 Diffuse Reflectance Spectroscopy (DRS)

The optical property of the SnS_2 NSs was characterized using UV-vis diffuse reflectance spectrometer using $BaSO_4$ as a reference. Figure 3.3a displays that the onset of the absorption started from 700 nm with strong absorption starting at ~ 550 nm, indicating the absorption of the SnS_2 NSs in the visible range. The optical band gap was calculated using the following tauc equation

$$\alpha h\nu = A(h\nu - E_g)^{n/2}$$

A = constant, $h\nu$ = light energy, E_g = optical band gap, α = measured absorption coefficient. In the above equation, n tells us about the characteristics of the semiconductor, n=1 for direct transition and n=4 for an indirect transition. The prepared SnS_2 NSs shows the direct

transition. In Figure 3.3a, the optical absorbance spectrum of SnS_2 is shown. The semiconductor shows absorption in the visible light range, and a steep absorption edge falls in the visible region of the spectrum. Figure 3.3b shows the Tauc plot of prepared SnS_2, and a bandgap of around 2.2 eV is obtained.

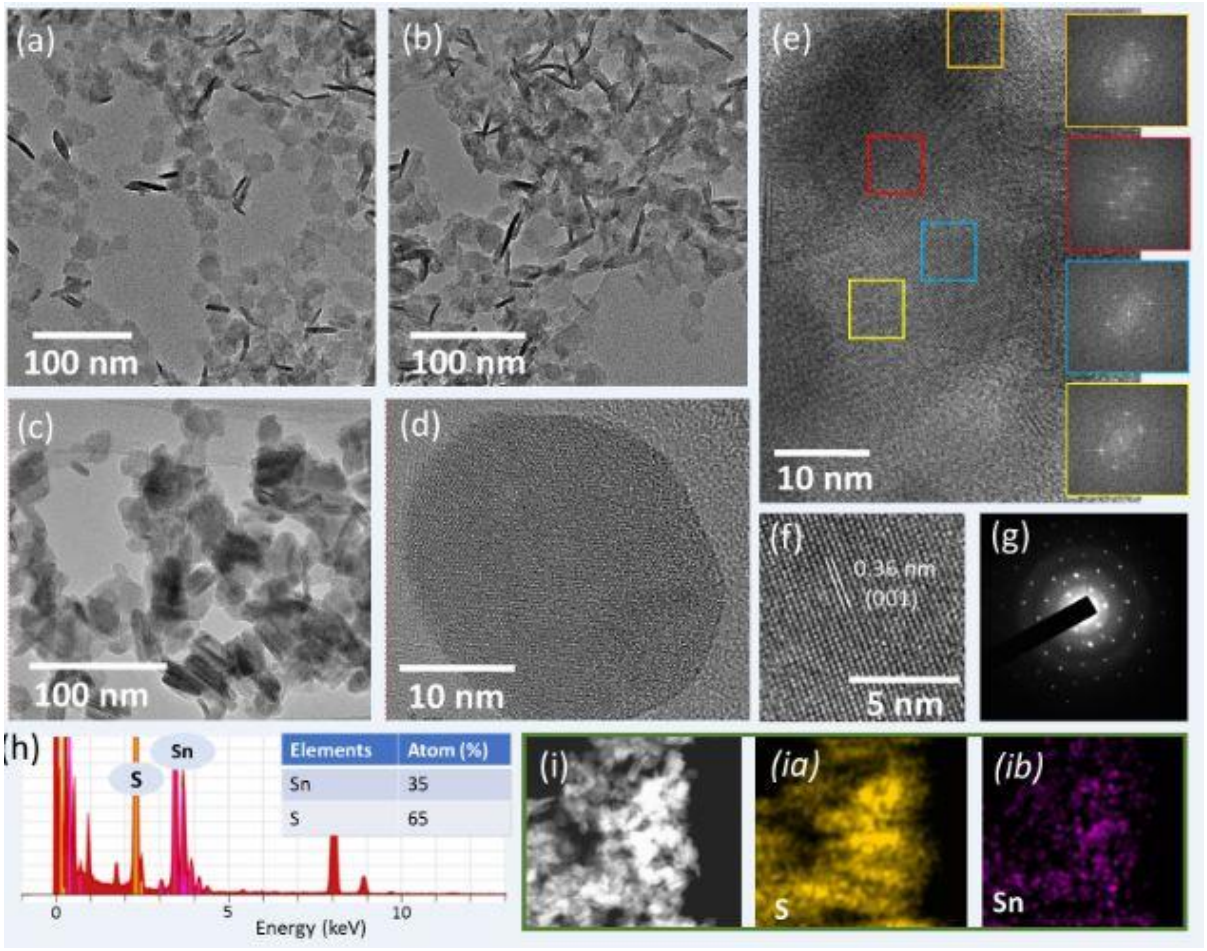

Figure 3.2 – (a, b, c) TEM images of SnS_2 NSs. (d) TEM image of a single SnS_2 NS showing their typical size (~25 nm). (e) High magnification-TEM image of a larger SnS_2 NS at a higher resolution. FFT patterns were generated from various parts of the image, showing that even though the crystallinity does not appear uniform throughout, the sheet has the same crystal-orientation in all places within a nanosheet. (f) HRTEM image of a NS showing the (001) crystal planes of SnS_2. (g) SAED pattern of a single SnS_2 NS along the (001) zone axis. (h) EDS spectrum and (i) elemental mapping images of the as-synthesized SnS_2 NSs.

:

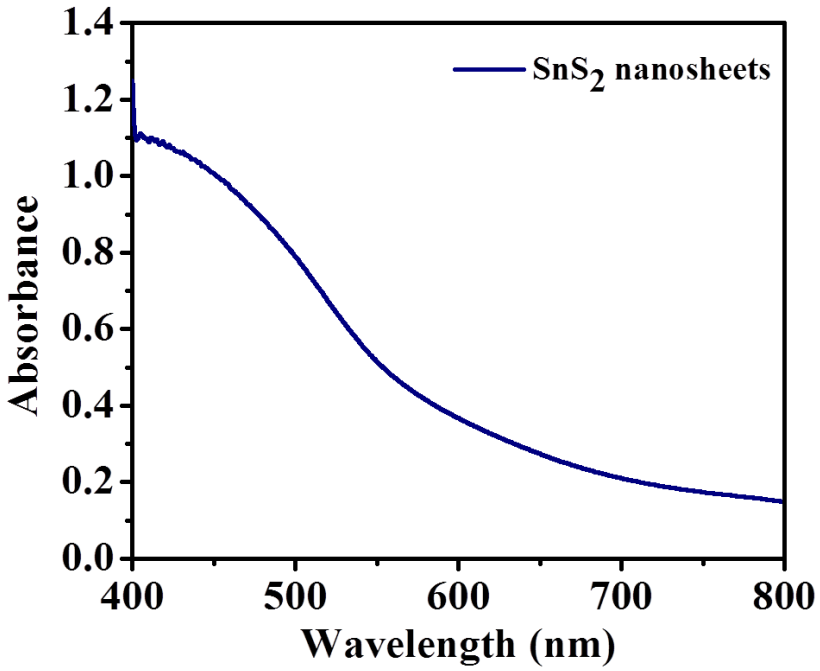

Figure 3.3a- DRS plot of prepared SnS_2 NSs

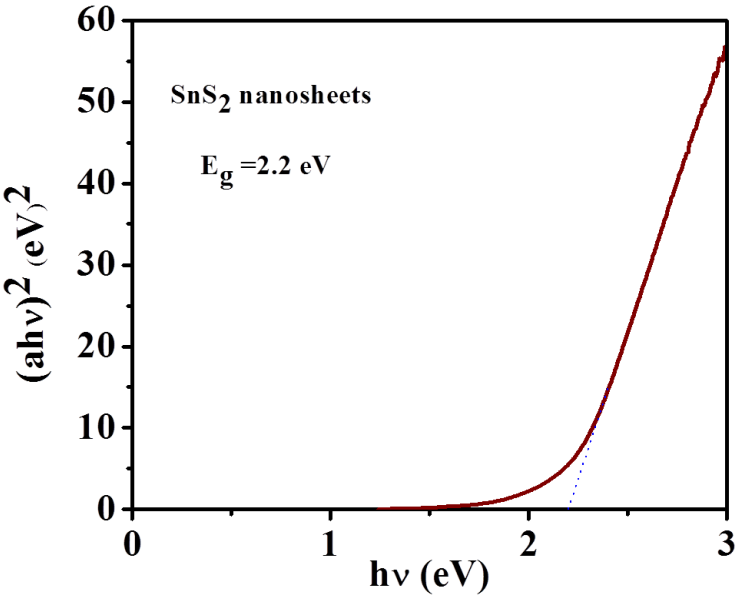

Figure 3.3b- Tauc plot showing the bandgap (E_g)

3.1.4 BET surface area

The BET specific surface area of the SnS_2 NSs was determined by N_2 adsorption, as shown in Figure 3.4, and the obtained surface area is 88.2 m^2/g. Figure 3.4a shows the nitrogen adsorption-desorption isotherm of as-synthesized SnS_2 NSs, where it is observed that it exhibits type IV isotherm with a hysteresis loop[28].

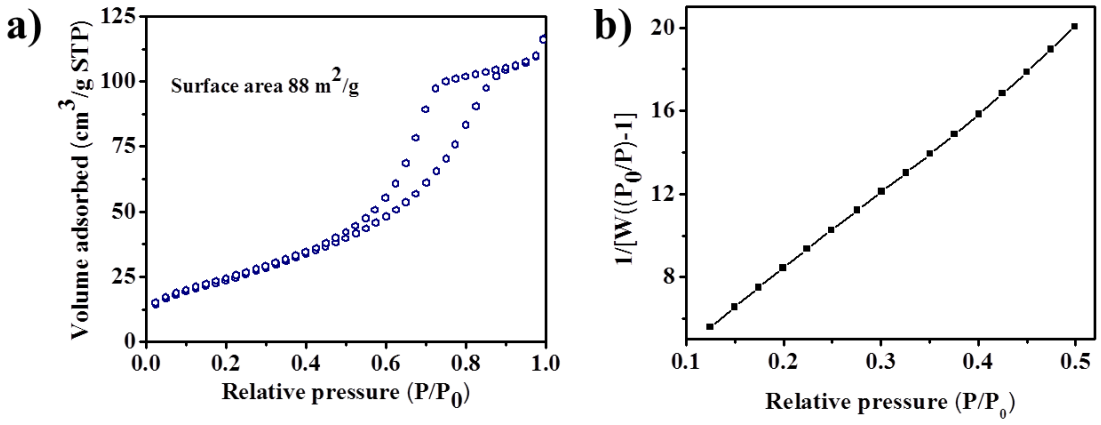

Figure 3.4a) Nitrogen adsorption-desorption isotherm of as-prepared SnS_2 NSs. Figure 3.4b) Multipoint BET plot.

3.2 Adsorptive activity of SnS_2 NSs in RhB and MB

Effect of initial concentration

The adsorption performance of SnS_2 was studied using different concentrations of RhB and MB dyes. 4 different concentrations of 50 mL RhB solutions were prepared-15µM, 20µM, 25µM, 30µM, and the adsorption property was observed using 15 mg of prepared SnS_2 NSs catalyst. Figure 3.5 shows the absorbance versus wavelength plots of 15µM, 20µM, 25µM, 30µM RhB solutions with SnS_2 NSs during 1 hr adsorption in the dark. Absorption maximum appears at 553-554nm.

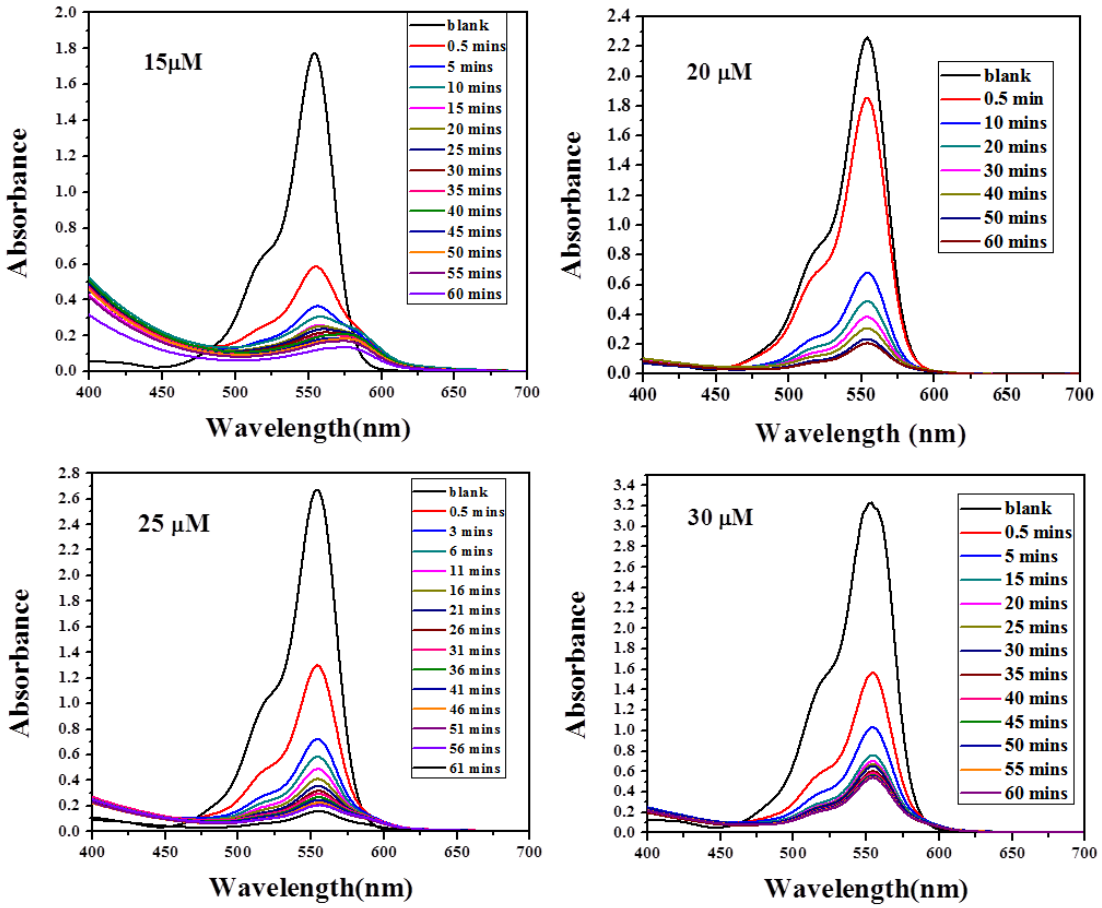

Figure 3.5- Absorbance vs. wavelength plots of RhB solutions

From Figure 3.5, we can see that SnS_2 NSs adsorbs almost 70% during the first 5 minutes and reaches equilibrium adsorption capacity at 60 minutes. In the case of 15μM, we can see some peak shifting from 553nm as the duration of adsorption increases but 20μM, 25μM and 30μM solutions of RhB showed regular adsorption with the increase of time. SnS_2 NSs adsorbs about 91%, 91%, 94%, and 83% RhB from 15μM, 20μM, 25μM, and 30μM solution respectively in 1 hr as can be seen from Figure 3.6. Figure 3.7 shows the change of equilibrium adsorption capacity with concentration and it increases with the increase of concentration. This implies that the removal of RhB dye decreases with concentration. It means that the adsorption of dye is highly dependent on the initial concentration of dye. It is because of the fact that at lower concentrations, the ratio of the initial number of RhB dye molecules to the available surface area is low; subsequently, the fractional adsorption

becomes independent of initial concentration. However, at higher concentrations, the available sites of adsorption become fewer, and hence the percentage removal of RhB dye depends upon initial concentration[72].

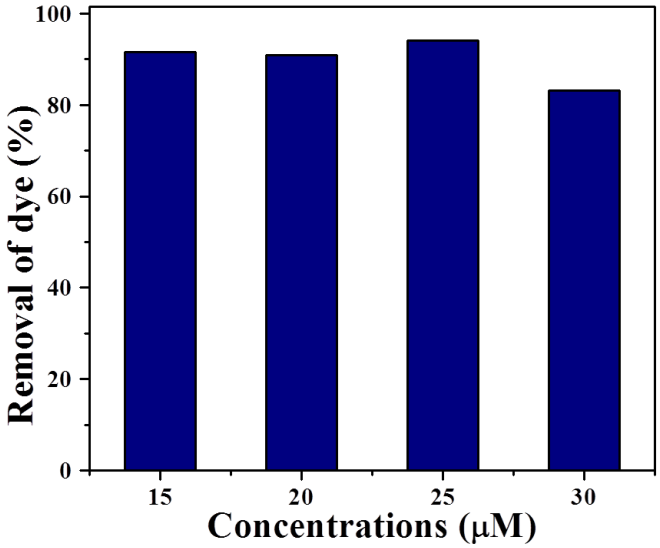

Figure 3.6- Removal of dye % in different concentrations of RhB solution

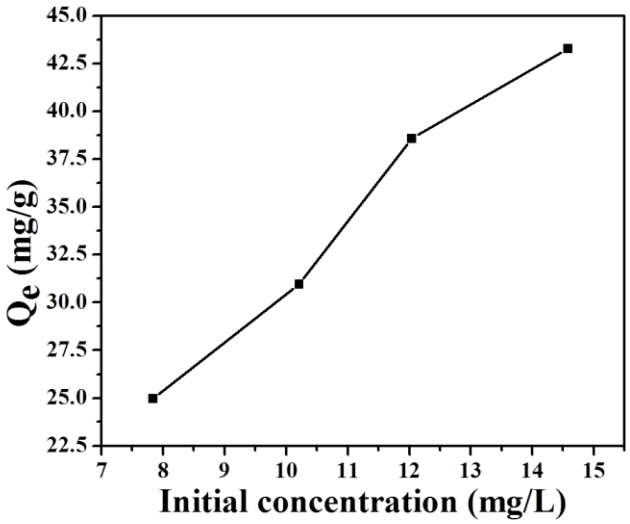

Figure 3.7- Equilibrium adsorption capacity (Q_e) versus initial concentration of RhB

Figure 3.8 shows the change in adsorption capacity (Q_t) with an increase in contact time. Equilibrium has established at 5 minutes with a slow increase in adsorption capacity up to 60 minutes. The curves are smooth, continuous, and single, leading to saturation suggesting the possible monolayer RhB coverage on the surface of SnS_2 nanosheets[73].

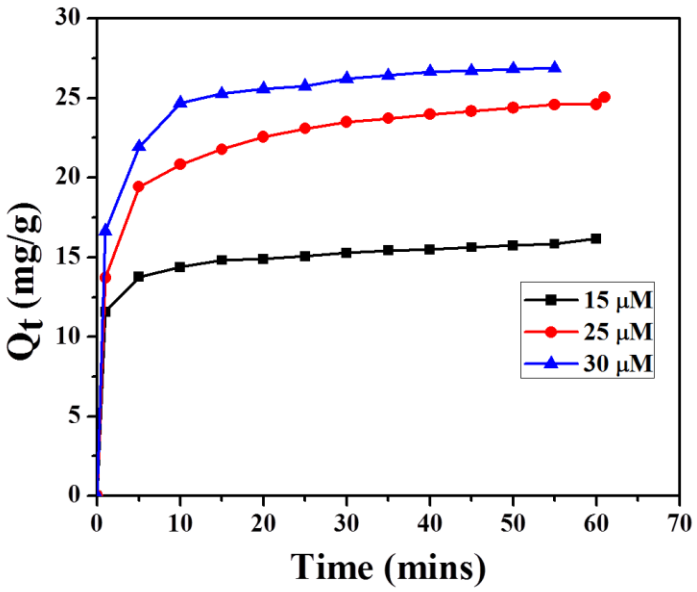

Figure 3.8- Effect of adsorption capacity (Q_t) with contact time (minutes)(RhB)

In the case of MB, 5 different concentrations were prepared to study the concentration-effect-10µM, 15µM, 20µM, 25µM, and 30µM 50 mL each. 15 mg of prepared SnS_2 NSs was used in each case. Figure 3.9 shows the absorbance plots of each concentration with wavelength. An absorption maximum appears at 664.7nm. Rapid adsorption happens in the first 30-60 secs of stirring. In 10µM, 15µM, and 20µM MB solutions, the dye was almost adsorbed totally within 15 minutes of stirring in the dark. It took 30 minutes to reach the saturation point of adsorption in 25µM, and 30µM solutions. Because of its efficient adsorption, we performed a recyclability experiment to observe up to how many cycles the same amount of catalyst can serve as an adsorbent. We used 15 mg of catalyst, and after each cycle, the catalyst was washed with distilled water and ethanol to remove the adsorbed dye and reused again. However, there has been considerable loss of the catalyst during the washing

procedure because the catalyst consists of 25-30nm size sheets, which make it difficult to collect.

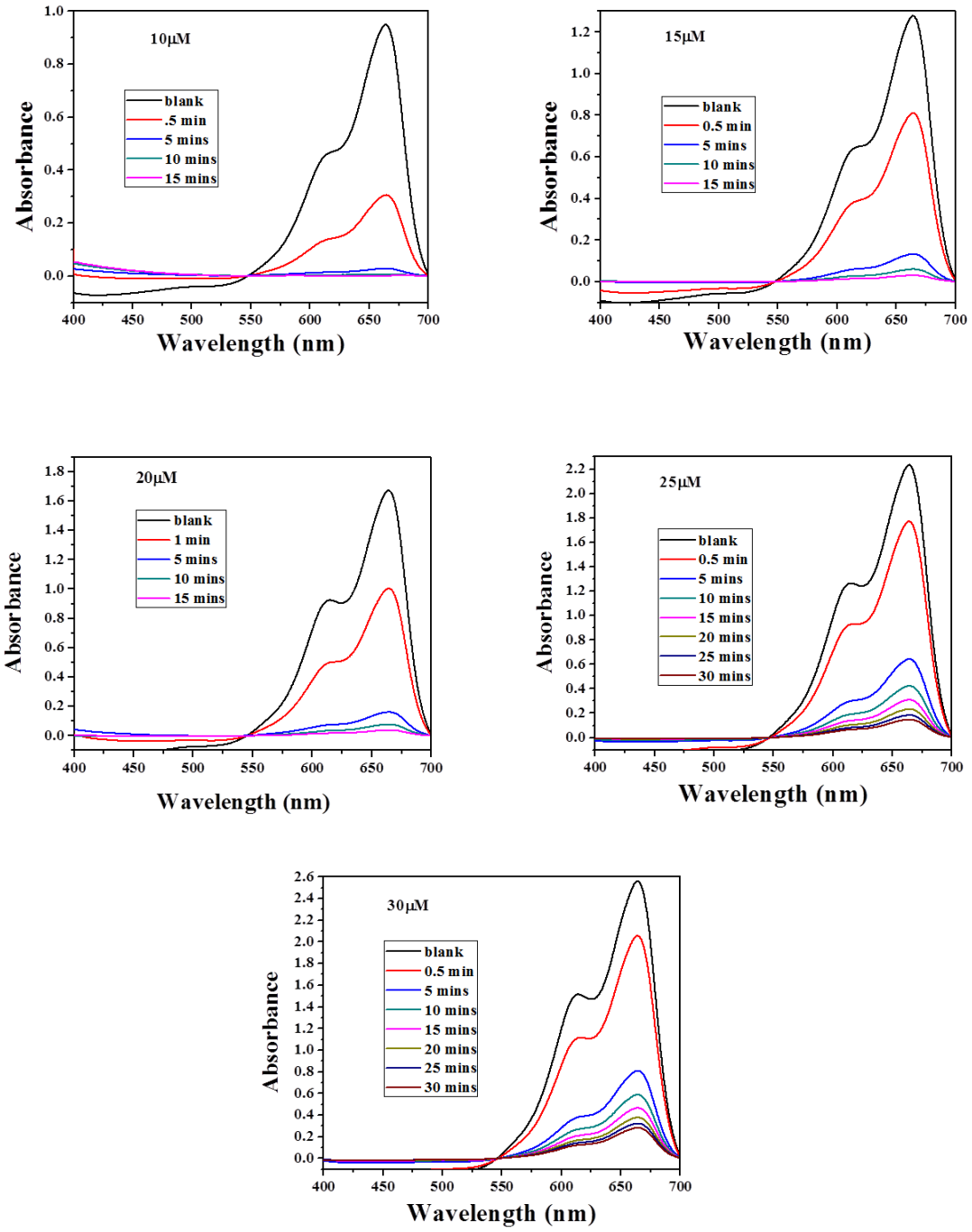

Figure 3.9- Absorbance vs. wavelength plots of MB solutions

Figure 3.10 shows the recyclability plot up to 5 cycles. We can see that the catalyst is able to adsorb up to 90% until the 5th cycle, which implies its efficiency.

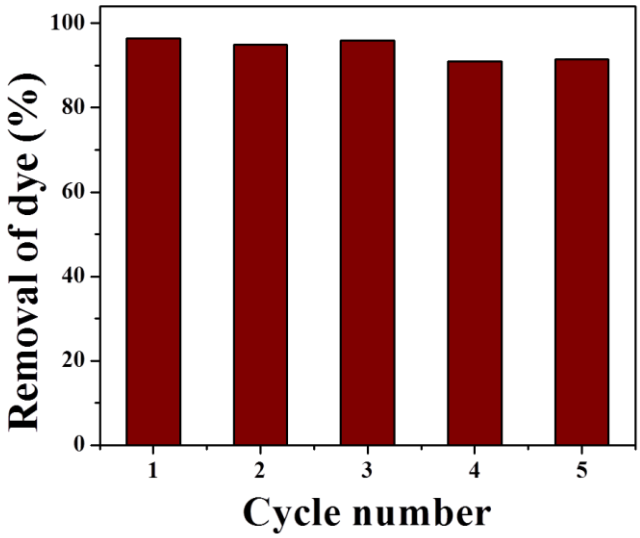

Figure 3.10- Recyclability plot of MB dye by SnS_2 NSs.

Figure 3.11 shows the percentage of removal of MB dye in each concentration. In 10μM, it shows 99.9% removal of MB dye. However, as concentrations increase, the rate of removal decreases but still adsorbs more than 85%.

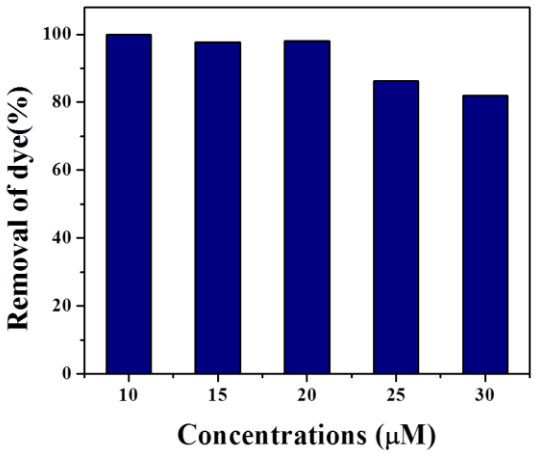

Figure 3.11- Removal of dye (%) in different concentrations of MB solutions.

Figure 3.12 shows the change in equilibrium adsorption capacity with initial concentration. The trend shows the same behavior as that of RhB dye. The value Q_e increases with concentration revealing that the removal of dye decreases with an increase in concentration.

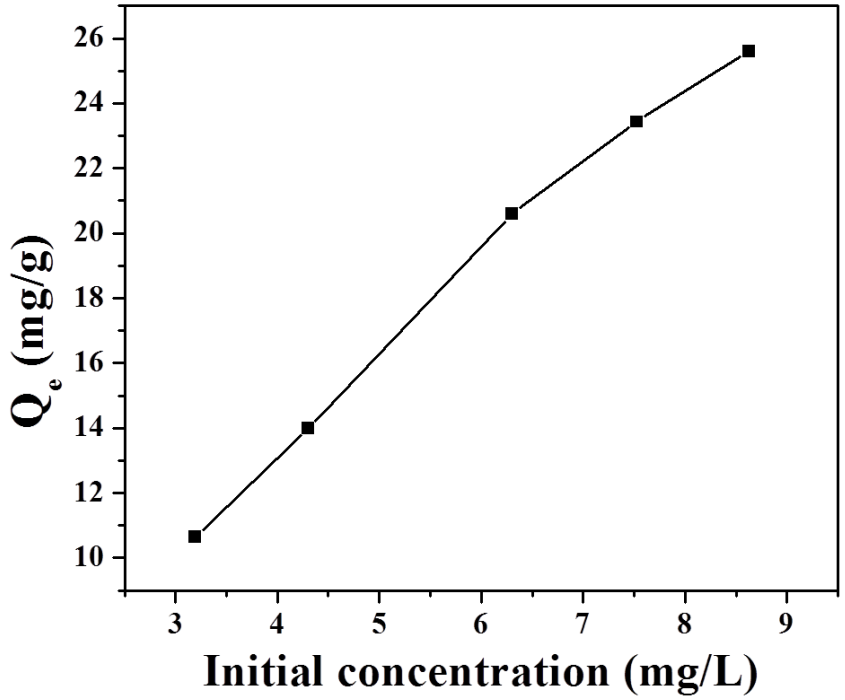

Figure 3.12- Equilibrium adsorption capacity (Q_e) versus initial concentration of MB

When the values of Q_e of RhB and MB with respect to concentrations were compared, the Q_e value of RhB is slightly higher than that of MB. The value of Q_e of 30μM MB is 25.6 mg/g, and that of 30μM RhB is 43.3 mg/g. Therefore, the prepared SnS_2 nanosheets will be useful for the adsorption of cationic dyes.

Figure 3.13 shows the change in adsorption capacity (Q_t) with an increase in contact time. Equilibrium has established at 5 minutes with a slow increase in adsorption capacity up to 15 minutes in case of lower concentrations and 30 minutes in higher concentrations. The curves are smooth, continuous and single, leading to saturation suggesting the possible monolayer MB coverage on the surface of SnS_2 nanosheets[73], which is same as that of RhB adsorption.

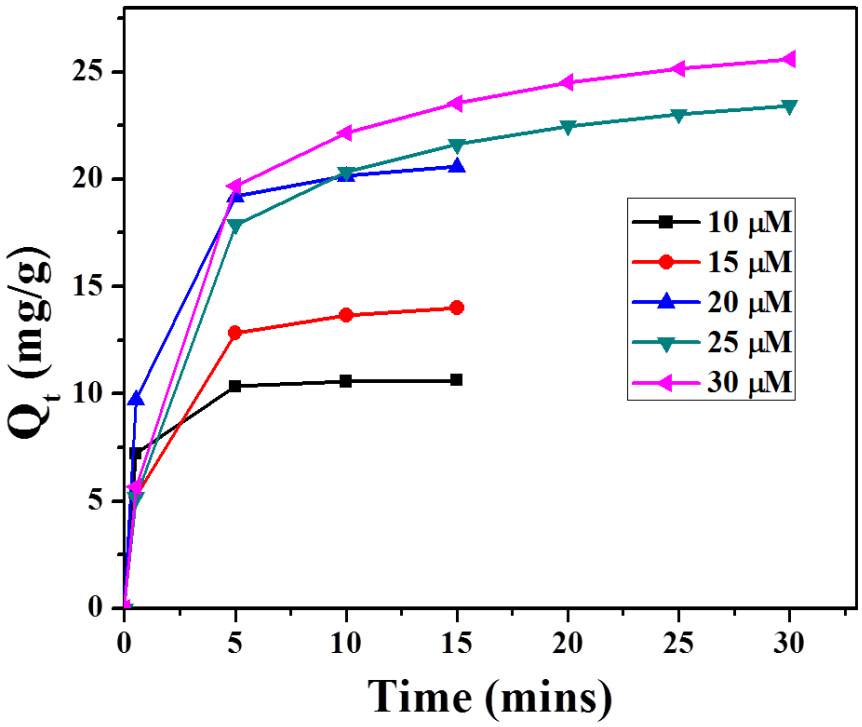

Figure 3.13- Effect of adsorption capacity (Q_t) with contact time (minutes)(MB).

Effect of pH

The pH parameter is a significant factor for the adsorption properties of dye by affecting both the existing forms of the dye molecules and the charged species and density on the surface of SnS_2 nanosheets. We expected the SnS_2 surface to be negatively charged since it adsorbs cationic dyes so effectively, so we studied pH effect on adsorption capacity at pH 2.0 to 11.0. The effect of different pH on adsorption has also been observed in a particular concentration of RhB solution (25µM). The different pH considered are- 2.03, 7.4, 9.33, 10.95, and 11.01. The pHs were adjusted using HCl and NaOH solution. In pH-2.03, 7.4, and 9.33, the adsorption happened with a continuous decrease in the intensity of RhB. However, in pH 10.95 and 11.01, we observed a major change in the absorbance spectra. Immediately after the start of the stirring of the solution mixture, the major peak at 553nm disappears, and two new peaks appear at 559nm and 575nm with disordered adsorption behavior. It may be

because of the dissociation of RhB at the basic condition that causes certain disturbances on the catalyst surface, therefore, being unable to adsorb the dye properly. Therefore, we could not obtain data points for pH=10.95 and pH=11.01. Figure 3.14 shows the absorption spectra at different pH of RhB solutions.

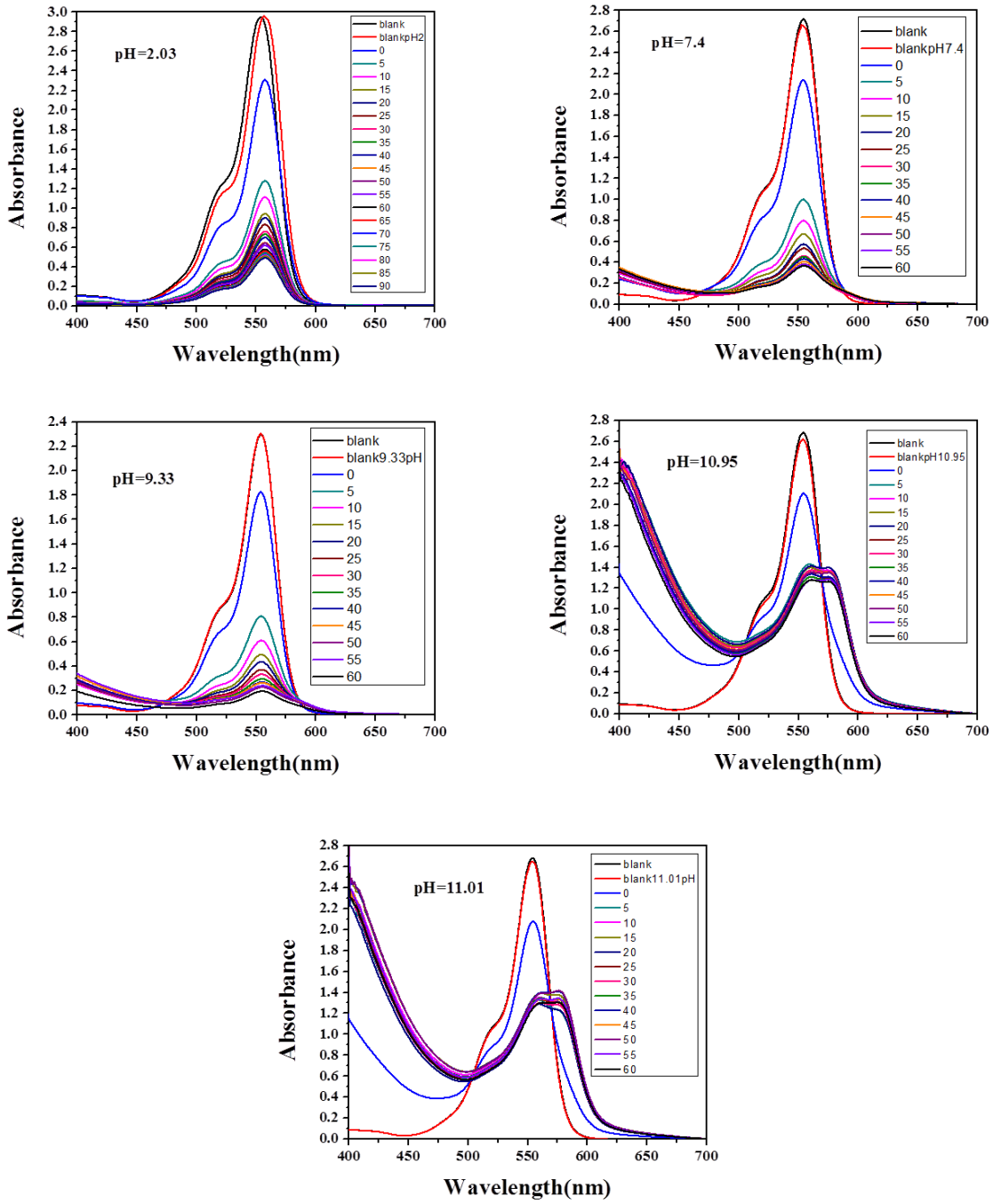

Figure 3.14- Time-dependent UV-Vis spectra at different pH of RhB.

Figure 3.15 shows the adsorption capacity with an increase in pH. The highest adsorption capacity-23.67 mg/g is found at pH=2.03, in acidic medium, and it gradually decreases to 21.1mg/g in basic medium. It could imply that at pH<7, RhB molecules exhibit a cationic form to promote electrostatic interactions between the SnS_2 surface and RhB.

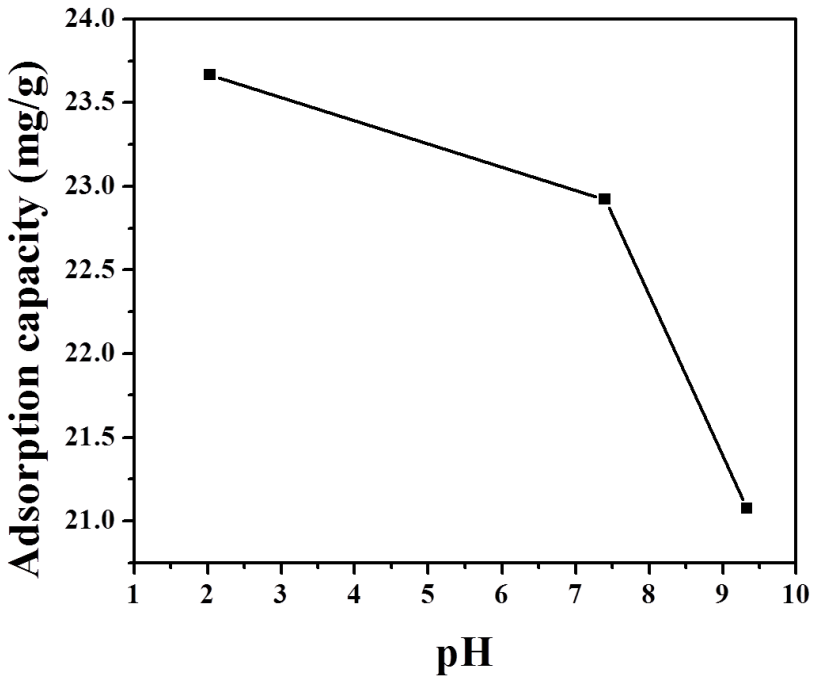

Figure 3.15- Adsorption capacity vs. pH in the case of RhB.

To investigate the effect of pH on MB adsorption on the SnS_2 surface, we considered the following set of pHs- 2.84, 4.06, 7, 9.56, and 11.35. Figure 3.16 shows the absorption spectra of MB solutions of different pHs. 20μM of MB solution was used in each case with 15 mg of catalyst. From this figure, it is evident that the adsorption is better in the basic conditions. In acidic medium, the catalyst takes almost 30 minutes to adsorb 91% of dye. So, the adsorption rate decreases in the acidic medium when compared to the neutral medium where the removal is up to 98% after 15 minutes. In 11.35 pH solution, the solution turned green after 15 minutes adsorption and there is no absorbance at 664.7nm. Therefore, the adsorption rate increases in the basic medium up to 100% removal of dye, and probably there is the dissociation of MB in higher basic condition.

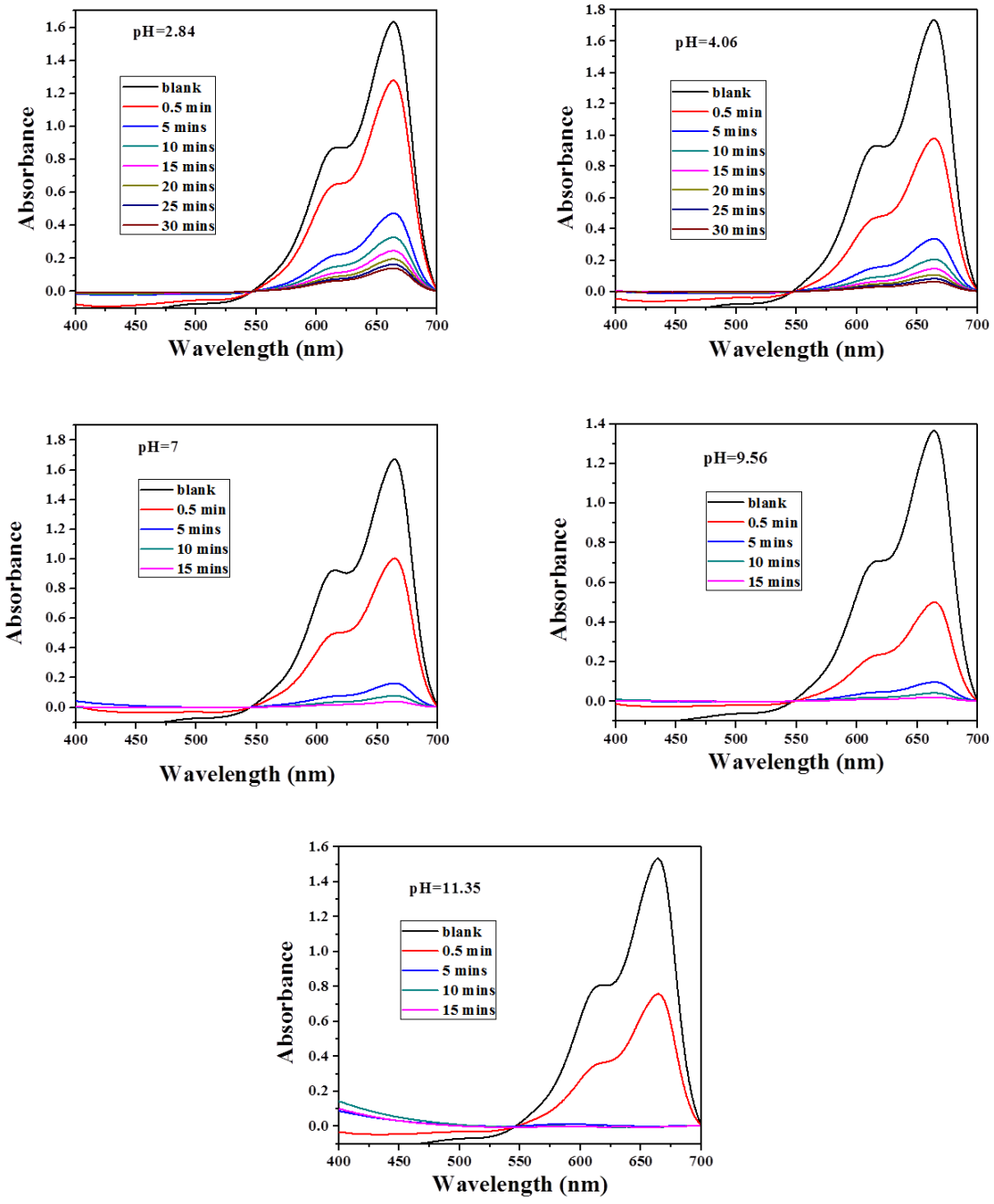

Figure 3.16-Time-dependent UV-Vis spectra at different pH of MB

Figure 3.17 shows the change in adsorption capacity with an increase in pH. In this graph, we can see that the adsorption capacity increases with an increase in pH which means more

adsorption. This can be explained in the way that when the pH is less, the surface of the adsorbent becomes more positive thus causing a decrease in adsorbing cationic dyes. Whereas, when at higher pH, the surface of SnS_2 becomes more negative hence more amount of dye adsorbed, consequently taking less time to adsorb the total concentration of dye.

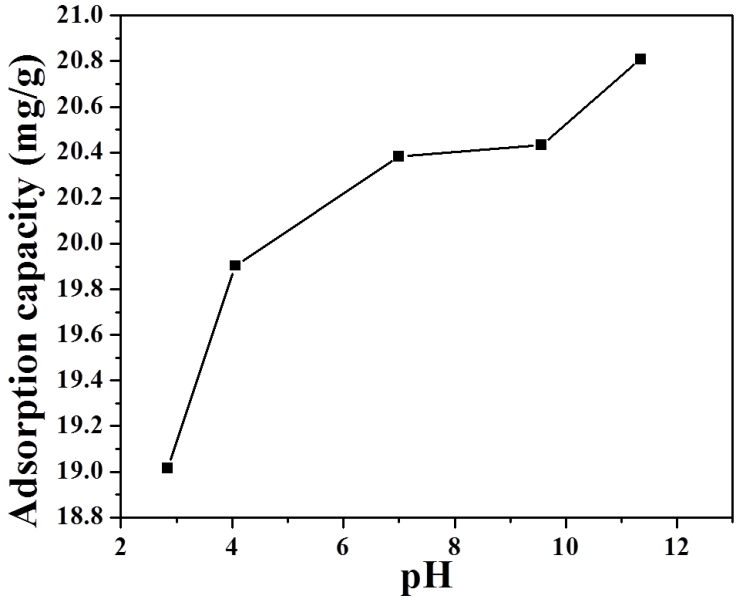

Figure 3.17- Adsorption capacity vs. pH in case of MB

Kinetics study

The adsorption mechanism of dyes onto the surface of adsorbents can be illustrated by the adsorption kinetics model. During an adsorption process, external mass transfer in the bulk liquid phase, boundary layer diffusion and intraparticle mass transfer are three approaches. In order to investigate the mechanism, pseudo-first-order and pseudo-second-order kinetic models are adopted to examine the overall adsorption process. The experimental data were fitted in the kinetics equations.

Pseudo-first order: $\ln (Q_e-Q_t) = \ln Q_e - k_1 t$

Pseudo-second-order: $t/Q_t = 1/k_2Q_e^2 + t/Q_e$

Figure 3.18a shows the experimental data fitted in the pseudo-first-order kinetics model with R^2=0.9488 and the calculated adsorption capacity (Q_e)=3.18 mg g^{-1}. The value of k_1 is calculated to be 0.041. Figure 3.18b shows the pseudo-second-order kinetic model with R^2=0.9996 and calculated adsorption capacity (Q_e)=24.98 mg g^{-1}. The calculated value of k_2 is 0.05. Therefore, the pseudo-second-order kinetics fitting curve indicates a better relationship for the experimental data. Therefore, the adsorption of RhB dye onto the SnS_2 surface is due to the chemisorption and adsorption process that can be attributed to the electrostatic attraction between the negative charge on the surface of SnS_2 and RhB molecule[59].

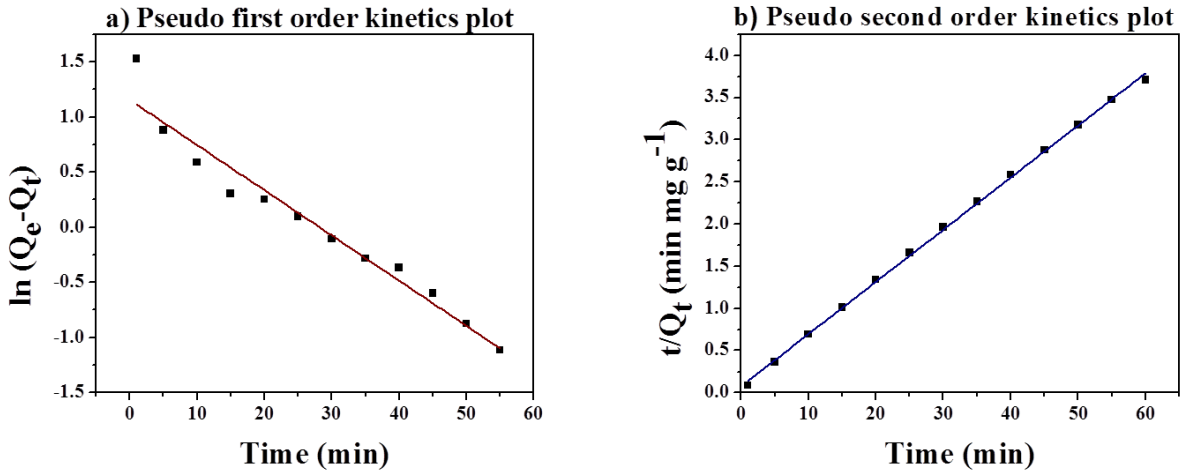

Figure 3.18-Kinetic adsorption data plots of RhB

The same kinetics study was conducted in the case of MB dye adsorption. Figure 3.19a shows the experimental data fitted in the pseudo-first-order kinetics model with R^2=0.90998 and the calculated adsorption capacity (Q_e) =8.345 mg g^{-1}. Figure 3.19b shows the pseudo-second-order kinetic model with R^2=0.9986 and calculated adsorption capacity (Q_e) =18.37mg/g, which is close to the actual adsorption capacity (17.27 mg/g). Therefore, the pseudo-second-order kinetics fitting curve indicates a better relationship for the experimental data. This implies that the adsorption of methylene blue on the surface of the SnS_2 NSs is due to chemical adsorption[59].

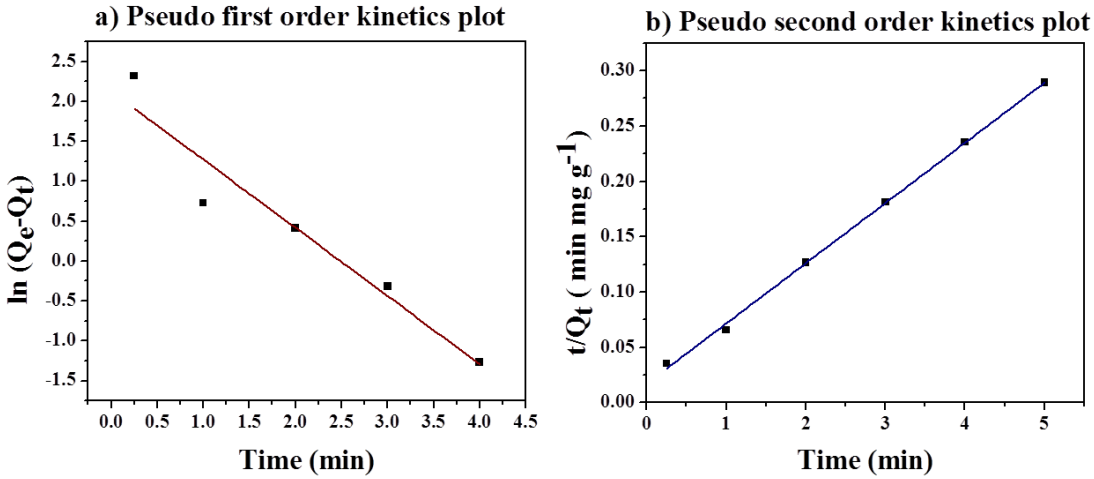

Figure 3.19-Kinetic adsorption data plots of MB

	RhB				**MB**			
	Q_e (mg/g)	**k_1/k_2**	**R^2**	**Q_{exp} (mg/g)**	**Q_e (mg/g)**	**k_1/k_2**	**R^2**	**Q_{exp} (mg/g)**
1^{st} order kinetics	3.18	0.041	0.9488		8.345	0.85411	0.90998	
2^{nd} order kinetics	24.98	0.05	0.9996	38.6	18.37	0.0171	0.9986	17.27

Table 3.1- Kinetic parameters of adsorption of RhB and MB by SnS_2 NSs

The relevant kinetic parameters of adsorption of RhB and MB dyes on SnS_2 nanosheet are complied in Table 3.1.

Adsorption Isotherms

The dye molecules distribution in the solid-liquid adsorption system at the equilibrium can be explained by adsorption isotherm. To comprehend the adsorption capacities and the arrangement of adsorbed molecules on prepared SnS_2 NSs surface, both the Langmuir isotherm model and the Freundlich isotherm model were used to analyze the obtained adsorption data. The Langmuir adsorption isotherm model assumes that monolayer adsorption takes place on the homogeneous adsorbent surface where the available active sites on the adsorbent are identical and energetically equivalent, and there is no interaction between the adsorbed molecules. The Freundlich adsorption isotherm model demonstrates the presence of heterogeneous adsorption surfaces with the interaction between adsorbed molecules. The experimental adsorption data of RhB and MB were fitted in the following equations:

Langmuir isotherm: $C_e/Q_e = C_e/Q_m + 1/k_LQ_m$

Freundlich isotherm: $\ln Q_e = \ln k_F + (1/n)\ln C_e$

Figure 3.20 shows the isotherm model in the case of RhB. Figure 3.20a shows the adsorption data fitted in the Langmuir isotherm model with R^2=0.9977 and calculated adsorption capacity (Q_m) from the slope = 53.28 mg/g. The value of k_L, calculated from the intercept, is 2.77 L/mg. The obtained values illustrate the adsorption process is well fit by the Langmuir isotherm model. The results show that RhB adsorption on SnS_2 nanosheets follows a single layer adsoprtion model with all the active sites on the adsorbent surface[17]. Figure 3.20b shows the data fitted in the Freundlich adsorption isotherm model with R^2=0.9298 and from the slope, we have the value of (1/n), which is less than 1 depicting that the adsorption process is favorable.

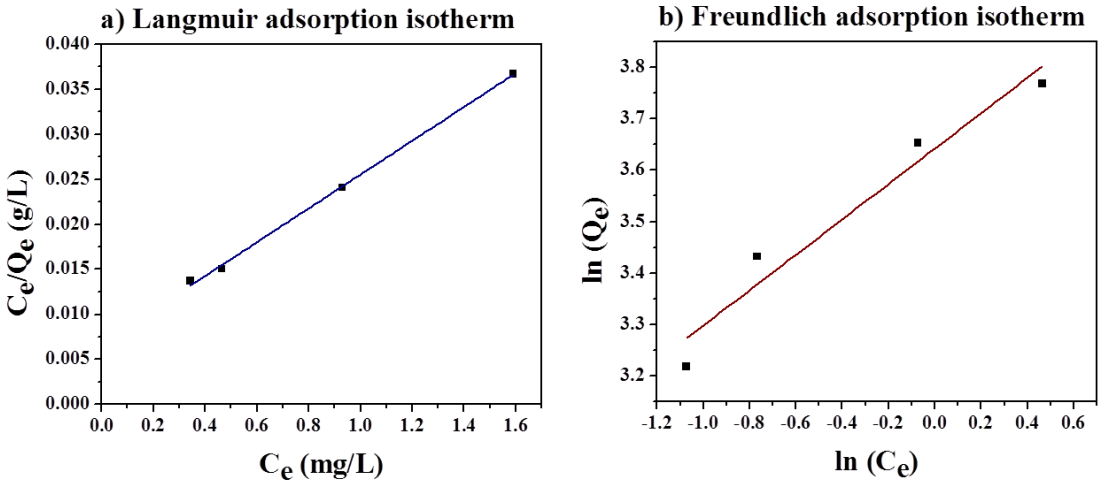

Figure 3.20- Adsorption isotherm models for RhB adsorption

The adsorption data of MB were plotted in the same isotherm models. Figure 3.21 shows the isotherm model in the case of MB. Figure 3.21a shows the adsorption data fitted in the Langmuir isotherm model with R^2=0.9905 and calculated adsorption capacity (Q_m) from the slope = 26.44 mg/g. The value of k_L, calculated from the intercept, is 22.51 L/mg. The results illustrate the adsorption process is well fit by the Langmuir isotherm model and MB adsorption on SnS_2 nanosheets conforms single layer adsoprtion model with all the active sites on the adsorbent surface. Figure 3.21b shows the data fitted in the Freundlich adsorption isotherm model with R^2=0.8152 and from the slope, we have the value of (1/n), which is less than 1 depicting that the adsorption process is favorable[59 17].

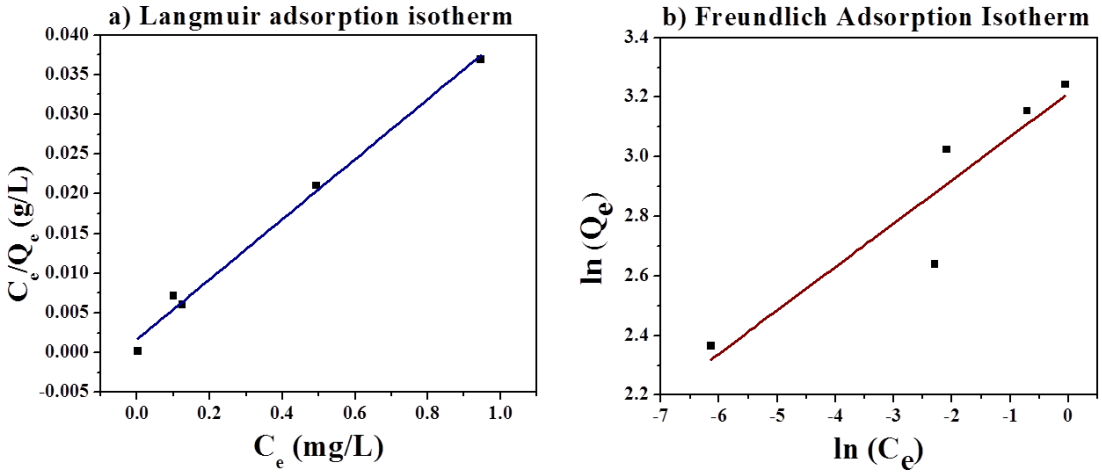

Figure 3.21- Adsorption isotherm models of MB

Table 3.2 shows the parameters of adsorption models of both RhB and MB dyes. Therefore, both the dyes follow Langmuir adsorption isotherm indicating the monolayer adsorption process.

Isotherms	**Langmuir**			**Freundlich**		
Parameters	Q_m (mg/g)	k_L (L/mg)	R^2	1/n	k_F (L/mg)	R^2
RhB	53.28	2.77	0.9977	0.34401	38.18	0.9298
MB	26.44	22.51	0.9905	0.1457	24.87	0.8152

Table 3.2- Value of parameters about RhB and MB adsorption isotherm models

The prepared SnS_2 nanosheets have higher adsorption capacity for RhB than that of MB. Table 3.3 and Table 3.4 display a list of adsorbents for RhB and MB, respectively for comparing obtained adsorption capacity (Q_m) values.

Sl.No	Catalyst	Q_m (mg/g)	Ref
1	Fe_3O_4/MoS_2 composites	24	[25]
2	MoS_2 nanosheets	76	[18]
3	MoS_2-glue sponge	123	[26]
4	SnS_2/MoS_2 Nanospheres	125	[17]
5	WO_3	64	[20]
6	SnS_2/rGO	94.07	[74]
7	$W_{18}O_{49}$ nanowires	120	[22]
8	ModifyingFe_3O_4 nanoparticles with humic acid	161.8	[75]
9	Fe_3O_4/rGO	142.86	[76]
10	Carbonaceous adsorbent	91.9	[77]
11	Tannery residual biomass (TRB)	213	[78]
12	Fe_3O_4/AC	182.48	[79]
13	Activated C	60.8	[73]
14	Sodium montmorillonite	38.27	[80]
15	SnS_2	53	This work

Table 3.3- Adsorption capacity for RhB of different materials

Sl.No	Catalyst	Q_m (mg/g)	Ref
1	Fe_3O_4/C	44.38	[81]
2	Graphene oxide-calcium alginate composites	181.81	[14]
3	CNTs wrapped with poly (sodium 4-styrene sulfonate)	100	[82]
4	Sodium alginate electrospun nanofibre membranes	2357.87	[83]
5	ZnS,Cu-NP-AC	123.5	[84]
6	Polyaniline-TiO_2 hydrate	458.10	[85]
7	Activated carbon (EFB-UAC)	435	[86]
8	Natural zeolite	21	[16]
9	Graphene oxide	1939	[13]
10	Graphene-magnetite composite	43.82	[15]
11	SnS_2	26.44	This work

Table 3.4- Adsorption capacity for MB of different materials

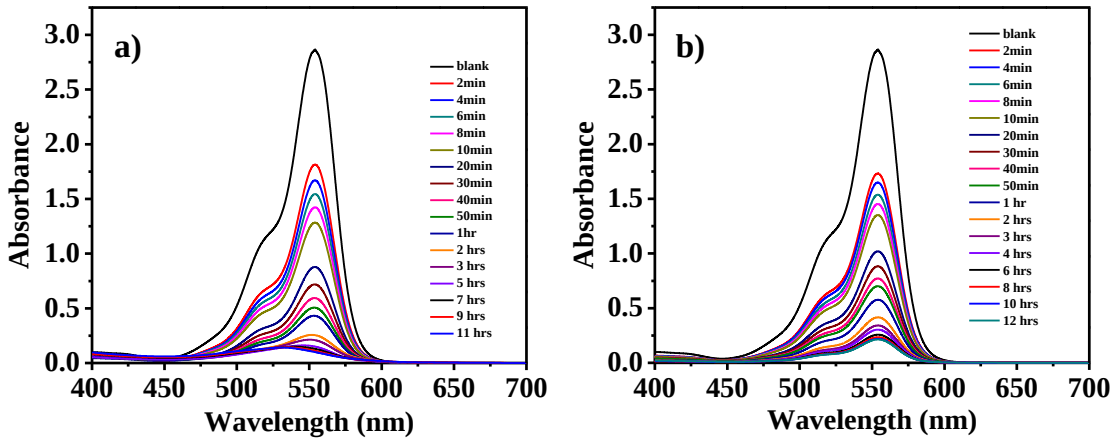

Figure 3.22- a) Time-dependent of the UV-Vis spectrum of RhB photocatalytic degradation by SnS_2 NSs. b) Time-dependent UV-Vis spectrum of adsorption of RhB by SnS_2 NSs in the dark.

It is already known from previous literature that SnS_2 is capable of degrading organic dyes in the presence of light. To investigate the photocatalytic degradation activity of the prepared SnS_2 NSs, we prepared a definite concentration (25μM, 50 mL) of RhB dye and added 15 mg of our catalyst. Figure 3.22 shows the time-dependent absorption spectra of RhB with SnS_2 NSs in both light and dark. It is observed that our prepared catalyst shows minimal degradation and adsorption is its dominant property of SnS_2 NSs. The RhB degradation initiated after 7 hrs of irradiation with a shift in absorption maximum at ~ 531 nm where the de-ethylation process may have started. However, the dye degradation process is prolonged compared to other photocatalysts. Both the reactions were conducted up to 11-12 hrs.

To observe the adsorption process with anionic dyes, we did adsorption with methyl orange. We prepared 30μM (50 mL) solution of MO to which we added 15 mg of prepared SnS_2 NSs. Figure 3.23 shows the time-dependent UV-Vis spectrum of MO with SnS_2 NSs in dark as well as in presence of light. We can see that there is no adsorption in the first 60 minutes in dark condition showing SnS_2 NSs does not adsorb anionic dyes which suggests that the SnS_2 NSs have negative surface charge. When the reaction solution was put to light, it showed very slow degradation.

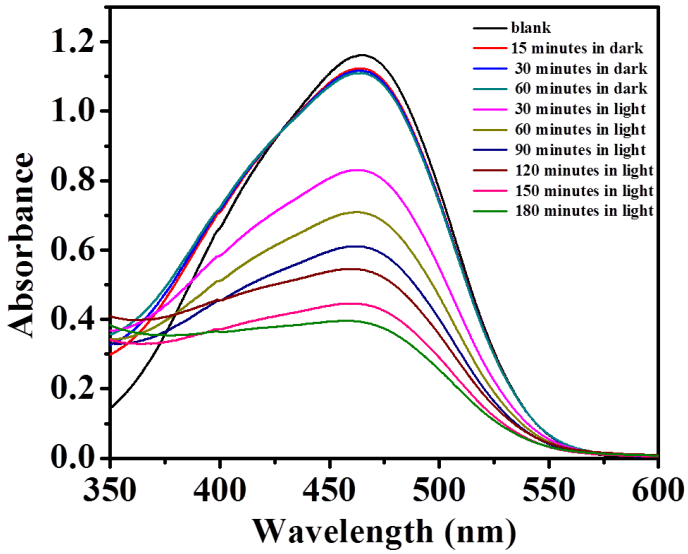

Figure 3.23- Time-dependent UV-Vis spectrum of MO with SnS_2 NSs

3.3 Photocatalytic activity- Cr-(VI) reduction by SnS_2 nanosheets

Photocatalytic Cr-(VI) reduction was performed in 400W xenon lamp using 25 mg of prepared SnS_2. 20ppm (25 mL) of $K_2Cr_2O_7$ was used as the initial concentration for reduction. Prior to illumination, Ar gas was purged to create an inert atmosphere. The adsorption-desorption equilibrium can be achieved within 30 minutes in the dark. During the reaction in light, the Cr-(VI) absorbance was measured by UV-Vis spectrometry at absorbance maxima at time intervals. Fig 3.24 shows the time-dependent UV-Vis spectrum, where we can see the reduction in Cr-(VI) absorbance intensities with time. It took 105 minutes for the completion of the reaction. The reduction ratio obtained is 93.6%. The photocatalytic rate constant was obtained using the following pseudo-first-order model-

$$\ln(C_0/C_t) = kt$$

where Co and Ct are the concentration of the reaction mixture at initial and t minutes respectively, k is the rate constant, and t is time (minutes). Figure 3.25 is the plot of ln (C_0/C_t) versus time (minutes), in which the k value was obtained from the slope of the linear plot. This indicates that the Cr-(VI) reduction follows a pseudo-first-order reaction in the presence of SnS_2 NSs, and the rate constant was found to be 0.032 min^{-1}.

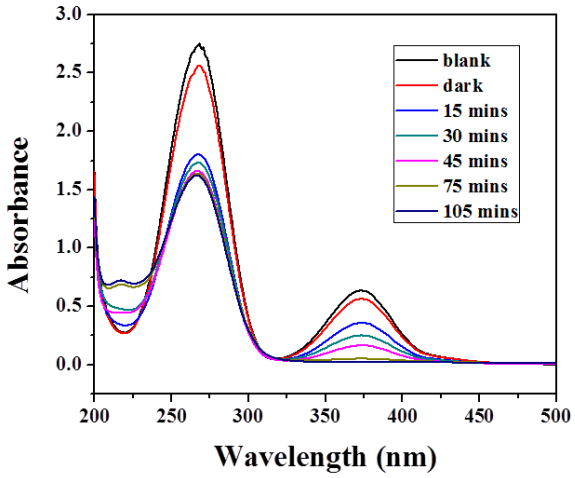

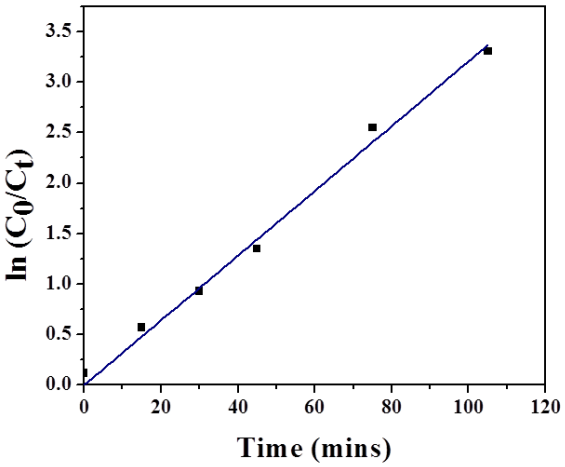

Figure 3.24- Time-dependent UV-Vis Spectrum.

Figure 3.25- Rate constant plot

Under visible light irradiation, the electrons in the valence band of SnS_2 NSs get excited to the conduction band and an equal number of photo-generated holes are obtained. Cr(VI) converts to Cr-(III) with the assistance of photo-generated electrons in the conduction band, and O_2 is produces with the help of H_2O in the valence band. Further, we performed a hole scavenger experiment to find the effect of the absence of holes. We took 35 mg of AO as a hole scavenger in 20 ppm of the $K_2Cr_2O_7$ solution. Figure 3.26 shows the time-dependent UV-Vis spectrum of the reaction in the presence of hole scavenger. It has been observed that the reaction proceeds faster than the previous case. We obtained a 95% removal of Cr-(VI) in 26 minutes of light irradiation. Figure 3.2 shows the rate constant plot of ln (C_0/C_t) versus time (minutes), in which the k value was obtained from the slope of the linear plot. This indicates that the Cr-(VI) reduction follows a pseudo-first-order reaction in the presence of SnS_2 NSs and AO, and the rate constant was found to be 0.1 min^{-1}.

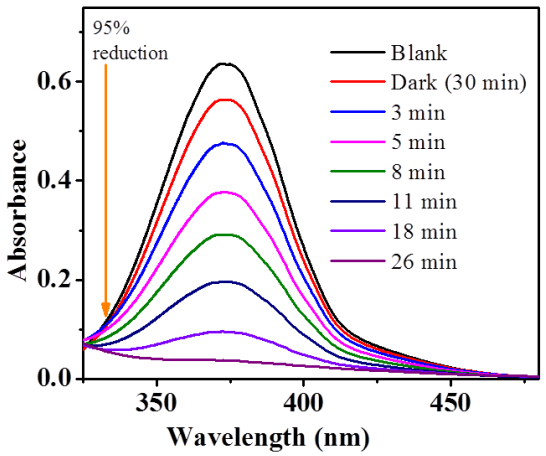

Figure 3.26- Time-dependent UV-Vis Spectrum. (in the presence of hole scavenger)

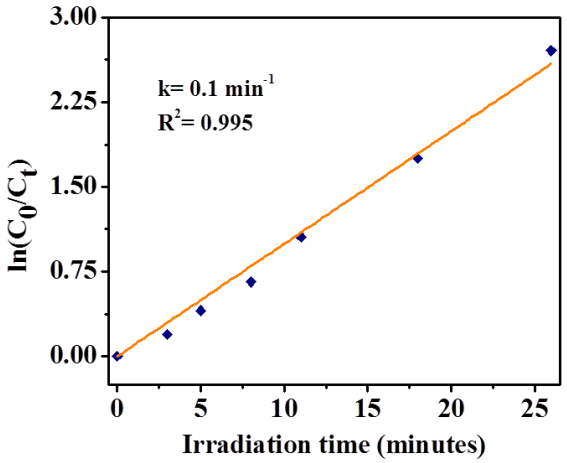

Figure 3.27- Rate constant plot (with AO)

Therefore the presence of hole scavenger enhances the rate of reaction and increases the reduction of Cr-(VI). In the presence of AO (hole scavenger), the holes are consumed by the electrons from hole scavenger; consequently, there is enhanced electron-hole separation facilitating the whole reaction. The reaction has been carried out in the sunlight and solar simulator under the same conditions, and 93% and 57% reduction in Cr-(VI) were observed respectively in 30 minutes. Figure 3.28a and b show the time-dependent UV-Vis spectra of the reaction in sunlight and solar simulator. Figure 3.29 shows the percentage reduction of Cr-(VI) in different light sources.

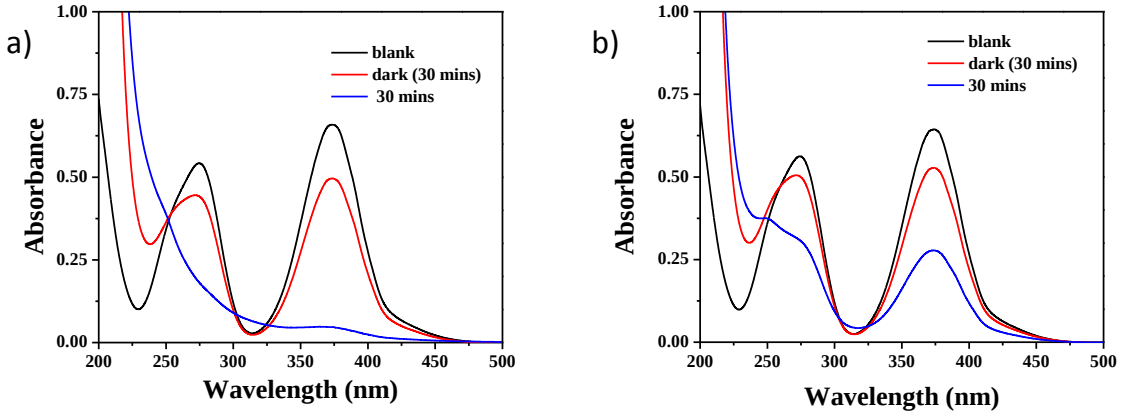

Figure 3.28a) Time-dependent UV-Vis Spectrum of Cr-(VI) reduction in sunlight. b) Time-dependent UV-Vis spectrum of Cr-(VI) reduction in solar simulator.

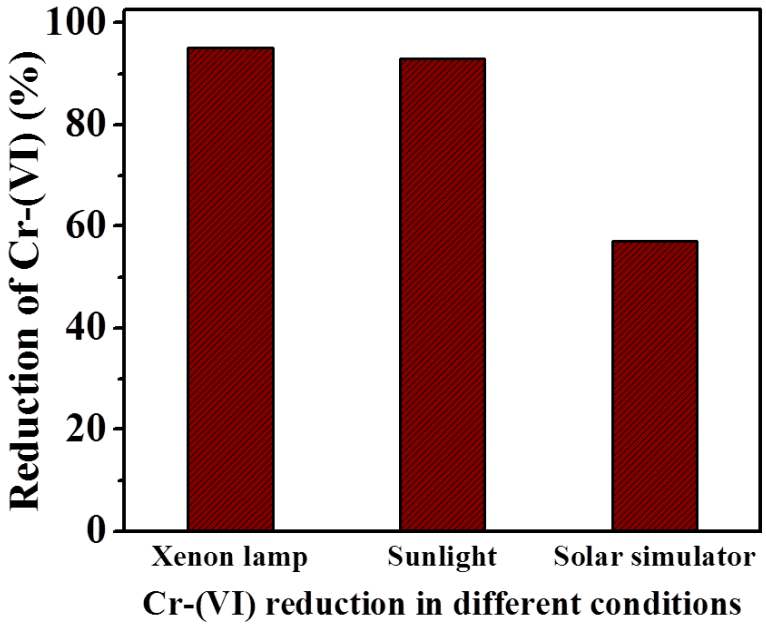

Figure 3.29- Cr-(VI) reduction in different light conditions.

The reduction of Cr-(VI) in sunlight is similar to that of the Xenon lamp. We have calculated the Apparent quantum efficiency (AQE) for the reactions in sunlight and solar simulator.

The AQE for the photocatalytic reduction of Cr-(VI) was calculated using the following expression:

$$AQE = n\,(No.of\ electron\ or\ hole) \times \frac{Number\ of\ Cr(III)\ molecule\ produced}{Number\ of\ incident\ photons} \times 100\ (\%)$$

When the reaction was carried out in direct sunlight, the AQE for SnS_2 NSs was found to be 0.0556%, and the AQE in the solar simulator using SnS_2 NSs was calculated to be 0.0362 %. Table 3.5 compares the photocatalytic reduction of Cr-(VI) of as-synthesized SnS_2 NSs with other SnS_2 composites and different catalysts.

Sl.No	**Catalyst**	**Dosage**	**Amt of reagent**	**DPC used**	**k (min^{-1})**	**time**	**Light source**	**SA (m^2/g)**	**Band gap (eV)**	**Reduction (%)**	**Ref**
1	SnS_2 NCs	300 mg	50 ppm 300 ml	Yes	0.0394	120 minutes	250 W Xe lamp (λ>420 nm)	82.4	2.27	99.6	[56]
2	NRG/SnO_2 /SnS_2	300 mg	50 ppm 300 ml	yes	0.102	30 minutes	λ>420 nm			92% up to 3rd cycle	[51]
3	TiO_2-RGO	20 mg	12 ppm 100ml	Yes		240 minutes	λ>450 nm	104.9		86.5	[35]
4	SnS_2-TiO_2	40 mg	100ppm 80 ml	Yes		100 minutes	300 Xe (λ>420 nm)	296		98	[39]
5	CM-n-TiO_2	2g/L	1-10ppm	Yes	0.0924	Up to 120 minutes	sunlight				[87]
6	SPNH-MOSF@SnS_2	50 mg	50 ppm 50 ml	Yes		90 minutes	300 W,((λ>400 nm)	103.85	2.1	99.9	[88]
7	NSC	10 mg	50ppm 50ml	Yes		120 minutes	150W xe,(λ>400 nm)		2.45	93	[89]
8	CoO MNA	15 mg	50 ppm 50 ml	Yes	0.0049	240 minutes	300 W	96	2.61	92 after 3 cycles	[47]
9	CuS NS	3 mg	10^{-4} M	Yes	0.076	60 mins	λ>420 nm		2.07		[46]

10	In-Zn(O,S)	20 mg	20ppm 50 ml	Yes	0.7423	3 minutes	500 W (λ>400 nm)		3.26	99.9	[50]
11	AgNPs/PSi	1g/L	30ppm 100 ml (citric acid=5mmol)	No		180 minutes	250W(λ>420 nm)			97.4	[90]
12	In^{3+}-doped SnS_2	100 mg	20ppm 250ml (acidic medium)	No	0.05	60 minutes	LED visible light	46.57	2	99.9	[91]
13	TiO2 NF-H	500 mg	40ppm 500 ml(in acidic medium)	Yes	0.0073	180 minutes	125W HP Hg lamp	44.9	3.24	75	[92]
14	TiO_2-5%rGO	100 mg	10ppm 150ml	yes		180 minutes	Xe lamp (λ>420 nm)	85.023	2.82	98	[37]
15	CdS/SnO_2	20 mg	10 ppm 50ml	yes	0.0581	20 minutes	300W Xe lamp(λ>420 nm)			95	[42]
16	$ZnFe_2O_4$/CdS NRs(7%)	25mg	100ppm 50 ml pH=2	no	0.0181	120 minutes	1kW Xe lamp (λ>420 nm)	106.8	2.16	90	[43]
17	MIL-53(Fe)/SnS [MS-15]	50 mg	20 ppm 50 ml	no	0.01878	60 minutes	300W Xe(λ>420 nm)	33.965		71.3	[44]
18	SnO_2/PANI-3%	300 mg	50ppm 300ml+1 ml 100mg/ml CA	yes	0.023	200 min	λ>420 nm	128.8		99.9	[93]
19	SnS_2-QDs/RGO	200 mg	100ppm	yes	0.025	120 min	300W Xe(λ>420 nm)	115.5		93.5	[45]
20	PPy/SnS_2	70mg	50ppm 70 ml	yes	0.0402	100 minutes	300W Xe(λ>420 nm)			99	[94]
21	SnS_2 nanosheets + AO	25 mg	20ppm 25 ml	no	0.1	26 minutes	400W Xe (λ>420 nm)	88.2	2.2	95	This work

Table 3.5- Comparison of Cr-(VI) reduction with other photocatalysts

The overall experiments- dye adsorption and Cr-(VI) reduction are explained schematically in Figure 3.30.

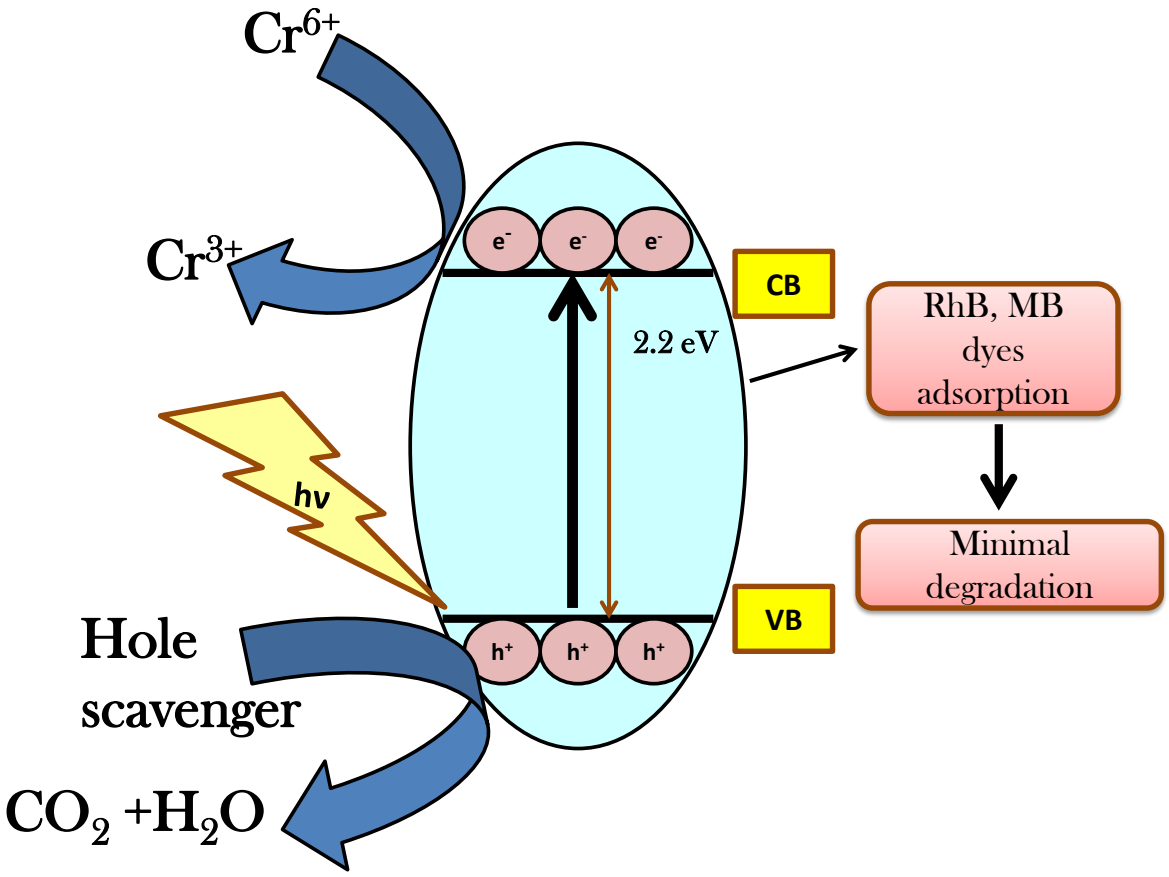

Figure 3.30- Schematic representation of dye adsorption and Cr-(VI) reduction by SnS_2 NSs.

4. CONCLUSION

In this study, SnS_2 nanosheets were synthesized using hydrothermal method. Tin-(IV) chloride and thioacetamide were used as reactants in our case. The synthesized SnS_2 nanosheets were characterized by PXRD, TEM, HRTEM, EDS, DRS, and BET. From the PXRD, it is observed that the prepared SnS_2 NSs are devoid of impurities; however, the intensities of 101, 102, and 103 peaks were weak which are predicted to be prominent with an increase in reaction temperature and duration. The TEM images show that the SnS_2 nanosheets are hexagonal of 25-30 nm in size. The EDS mapping displays a uniform distribution of Sn and S in SnS_2 NSs. The optical property was studied using DRS, and a bandgap of 2.2 eV was obtained. The as-synthesized SnS_2 NSs have a specific surface area of 88.2 m^2/g as obtained from BET measurements.

The as-synthesized SnS_2 NSs were used to adsorb cationic dyes RhB and MB dyes. Both the adsorption processes follow pseudo-second-order kinetics implying adsorption due to chemisorption and Langmuir adsorption isotherm model suggesting monolayer adsorption on the homogeneous adsorbent surface considering all the adsorption sites are similar and no interaction between adsorbed molecules. SnS_2 NSs showed 53.28 mg/g and 26.44 mg/g adsorption capacity for RhB and MB. The surface charge of SnS_2 NSs is believed to be negatively charged, which can be the reason for adsorbing cationic dyes and not adsorbing anionic dye-methyl orange. The effect of pH on adsorption was also studied. The basic medium seemed to be favorable for adsorption of MB dye onto SnS_2 NSs, unlike RhB, where the adsorption process becomes irregular at pH>10.

Photocatalytic reduction of Cr-(VI) was performed utilizing the as-synthesized SnS_2 NSs. The reaction was done in a 400W xenon lamp. The reaction, in the presence of ammonium oxalate as a hole scavenger, follows a linear fit in the pseudo-first-order model, and a rate constant of 0.1 min^{-1} was obtained.

The obtained SnS_2 NSs proved to be an efficient catalyst for dye removal and pollutant degradation. There is no release of unwanted chemicals, which makes the catalyst reliable for use.

5. SCOPE OF FUTURE WORK

The thesis attempted to investigate the adsorption and photocatalytic properties of SnS_2 NSs. The prepared SnS_2 NSs show a considerable amount of adsorption RhB and MB dyes. However, the photocatalytic degradation of these dyes is not achieved as expected. So, to use these SnS_2 NSs for photocatalytic dye degradation, we have to find out the answer to its minimal degradation according to which we can come up with different synthetic strategies. Also, for its usage in the industrial scale, we can modify the surface area of the SnS_2 NSs, which will lead to faster adsorption of dyes.

SnS_2 NSs have shown an efficient reduction of Cr-(VI) with a rate constant of 0.1 min^{-1}. We can improve the rate constant, which implies a faster reduction of Cr-(VI) to meet industrial demand.

6. BIBLIOGRAPHY

(1) Tan, K. B.; Vakili, M.; Horri, B. A.; Poh, P. E.; Abdullah, A. Z.; Salamatinia, B. Adsorption of Dyes by Nanomaterials: Recent Developments and Adsorption Mechanisms. *Sep. Purif. Technol.* **2015**, *150*, 229–242. https://doi.org/10.1016/j.seppur.2015.07.009.

(2) Kandisa, R. V.; Saibaba KV, N. Dye Removal by Adsorption: A Review. *J. Bioremediation Biodegrad.* **2016**, *07* (06). https://doi.org/10.4172/2155-6199.1000371.

(3) Foo, K. Y.; Hameed, B. H. An Overview of Dye Removal via Activated Carbon Adsorption Process. *Desalin. Water Treat.* **2010**, *19* (1–3), 255–274. https://doi.org/10.5004/dwt.2010.1214.

(4) Hassaan, M. A.; Nemr, A. El. Health and Environmental Impacts of Dyes : Mini Review. *Am. J. Environ. Sci. Eng.* **2017**, *1* (3), 64–67. https://doi.org/10.11648/j.ajese.20170103.11.

(5) Crini, G.; Lichtfouse, E. Advantages and Disadvantages of Techniques Used for Wastewater Treatment. *Environ. Chem. Lett.* **2019**, *17* (1), 145–155. https://doi.org/10.1007/s10311-018-0785-9.

(6) Franca, A. S.; Oliveira, L. S.; Ferreira, M. E. Kinetics and Equilibrium Studies of Methylene Blue Adsorption by Spent Coffee Grounds. *Desalination* **2009**, *249* (1), 267–272. https://doi.org/10.1016/j.desal.2008.11.017.

(7) Annadurai, G.; Juang, R. S.; Lee, D. J. Use of Cellulose-Based Wastes for Adsorption of Dyes from Aqueous Solutions. *J. Hazard. Mater.* **2002**, *92* (3), 263–274. https://doi.org/10.1016/S0304-3894(02)00017-1.

(8) Chcn, G.; Pan, J.; Han, B.; Yan, H. Adsorption of Methylene Blue on Montmorillonite. *J. Dispers. Sci. Technol.* **1999**, *20* (4), 1179–1187. https://doi.org/10.1080/01932699908943843.

(9) Bhattacharya, K. G.; Sharma, A. Kinetics and Thermodynamics of Methylene Blue

Adsorption on Neem (Azadirachta Indica) Leaf Powder. *Dye. Pigment.* **2005**, *65* (1), 51–59. https://doi.org/10.1016/j.dyepig.2004.06.016.

(10) Bulut, Y.; Aydin, H. A Kinetics and Thermodynamics Study of Methylene Blue Adsorption on Wheat Shells. *Desalination* **2006**, *194* (1–3), 259–267. https://doi.org/10.1016/j.desal.2005.10.032.

(11) Özer, D.; Dursun, G.; Özer, A. Methylene Blue Adsorption from Aqueous Solution by Dehydrated Peanut Hull. *J. Hazard. Mater.* **2007**, *144* (1–2), 171–179. https://doi.org/10.1016/j.jhazmat.2006.09.092.

(12) Han, R.; Wang, Y.; Han, P.; Shi, J.; Yang, J.; Lu, Y. Removal of Methylene Blue from Aqueous Solution by Chaff in Batch Mode. *J. Hazard. Mater.* **2006**, *137* (1), 550—557. https://doi.org/10.1016/j.jhazmat.2006.02.029.

(13) Zhang, W.; Zhou, C.; Zhou, W.; Lei, A.; Zhang, Q.; Wan, Q.; Zou, B. Fast and Considerable Adsorption of Methylene Blue Dye onto Graphene Oxide. *Bull. Environ. Contam. Toxicol.* **2011**, *87* (1), 86–90. https://doi.org/10.1007/s00128-011-0304-1.

(14) Li, Y.; Du, Q.; Liu, T.; Sun, J.; Wang, Y.; Wu, S.; Wang, Z.; Xia, Y.; Xia, L. Methylene Blue Adsorption on Graphene Oxide/Calcium Alginate Composites. *Carbohydr. Polym.* **2013**, *95* (1), 501–507. https://doi.org/10.1016/j.carbpol.2013.01.094.

(15) Ai, L.; Zhang, C.; Chen, Z. Removal of Methylene Blue from Aqueous Solution by a Solvothermal-Synthesized Graphene/Magnetite Composite. *J. Hazard. Mater.* **2011**, *192* (3), 1515–1524. https://doi.org/10.1016/j.jhazmat.2011.06.068.

(16) Han, R.; Zhang, J.; Han, P.; Wang, Y.; Zhao, Z.; Tang, M. Study of Equilibrium, Kinetic and Thermodynamic Parameters about Methylene Blue Adsorption onto Natural Zeolite. *Chem. Eng. J.* **2009**, *145* (3), 496–504. https://doi.org/10.1016/j.cej.2008.05.003.

(17) Cui, B.; Wang, Y.; Zhang, F.; Xiao, X.; Su, Z.; Dai, X.; Zhang, H.; Huang, S. Hydrothermal Synthesis of SnS2/MoS2 Nanospheres for Enhanced Adsorption

Capacity of Organic Dyes. *Mater. Res. Express* **2019**, *7* (1). https://doi.org/10.1088/2053-1591/ab5f24.

(18) Song, H. J.; You, S.; Jia, X. H. Synthesis of Fungus-like MoS2 Nanosheets with Ultrafast Adsorption Capacities toward Organic Dyes. *Appl. Phys. A Mater. Sci. Process.* **2015**, *121* (2), 541–548. https://doi.org/10.1007/s00339-015-9461-0.

(19) Saha, B.; Das, S.; Saikia, J.; Das, G. Preferential and Enhanced Adsorption of Different Dyes on Iron Oxide Nanoparticles: A Comparative Study. *J. Phys. Chem. C* **2011**, *115* (16), 8024–8033. https://doi.org/10.1021/jp109258f.

(20) Zhu, J.; Wang, S.; Xie, S.; Li, H. Hexagonal Single Crystal Growth of WO3 Nanorods along a [110] Axis with Enhanced Adsorption Capacity. *Chem. Commun.* **2011**, *47* (15), 4403–4405. https://doi.org/10.1039/c1cc00064k.

(21) Uddin, M. K.; Baig, U. Synthesis of Co3O4 Nanoparticles and Their Performance towards Methyl Orange Dye Removal: Characterisation, Adsorption and Response Surface Methodology. *J. Clean. Prod.* **2019**, *211*, 1141–1153. https://doi.org/10.1016/j.jclepro.2018.11.232.

(22) Gao, X.; Xiao, F.; Yang, C.; Wang, J.; Su, X. Hydrothermal Fabrication of W18O49 Nanowire Networks with Superior Performance for Water Treatment. *J. Mater. Chem. A* **2013**, *1* (19), 5831–5834. https://doi.org/10.1039/c3ta10724h.

(23) Tuzen, M.; Sarı, A.; Saleh, T. A. Response Surface Optimization, Kinetic and Thermodynamic Studies for Effective Removal of Rhodamine B by Magnetic AC/CeO2 Nanocomposite. *J. Environ. Manage.* **2018**, *206*, 170–177. https://doi.org/10.1016/j.jenvman.2017.10.016.

(24) Bian, X.; Lu, X.; Xue, Y.; Zhang, C.; Kong, L.; Wang, C. A Facile One-Pot Hydrothermal Method to Produce SnS2/Reduced Graphene Oxide with Flake-on-Sheet Structures and Their Application in the Removal of Dyes from Aqueous Solution. *J. Colloid Interface Sci.* **2013**, *406*, 37–43. https://doi.org/10.1016/j.jcis.2013.05.075.

(25) Song, H. J.; You, S.; Jia, X. H.; Yang, J. MoS2 Nanosheets Decorated with Magnetic Fe3O4 Nanoparticles and Their Ultrafast Adsorption for Wastewater Treatment. *Ceram. Int.* **2015**, *41* (10), 13896–13902. https://doi.org/10.1016/j.ceramint.2015.08.023.

(26) Fang, Y.; Huang, Q.; Liu, P.; Shi, J.; Xu, G. A Facile Dip-Coating Method for the Preparation of Separable MoS2 Sponges and Their High-Efficient Adsorption Behaviors of Rhodamine B. *Inorg. Chem. Front.* **2018**, *5* (4), 827–834. https://doi.org/10.1039/c8qi00012c.

(27) Zhang, G.; Du, X.; Wang, Y.; Wang, H.; Wang, W.; Fu, Z. Controllable Synthesis of SnS2 Nanostructures with High Adsorption and Photocatalytic Activities. *Mater. Sci. Semicond. Process.* **2017**, *64* (February), 77–84. https://doi.org/10.1016/j.mssp.2017.03.010.

(28) Wu, Z.; Xue, Y.; Zhang, Y.; Li, J.; Chen, T. SnS2 Nanosheet-Based Microstructures with High Adsorption Capabilities and Visible Light Photocatalytic Activities. *RSC Adv.* **2015**, *5* (31), 24640–24648. https://doi.org/10.1039/c5ra00395d.

(29) Wang, S. Solvothermal Synthesis of Porous SnS2 Nanotubes with Higher Adsorption and Photocatalytic Activity. *Surf. Sci.* **2019**, *690* (April). https://doi.org/10.1016/j.susc.2019.121469.

(30) Zhang, S.; Xu, W.; Zeng, M.; Li, J.; Xu, J.; Wang, X. Hierarchically Grown CdS/α-Fe2O3 Heterojunction Nanocomposites with Enhanced Visible-Light-Driven Photocatalytic Performance. *Dalt. Trans.* **2013**, *42* (37), 13417–13424. https://doi.org/10.1039/c3dt51492g.

(31) Naimi-Joubani, M.; Shirzad-Siboni, M.; Yang, J. K.; Gholami, M.; Farzadkia, M. Photocatalytic Reduction of Hexavalent Chromium with Illuminated ZnO/TiO2 Composite. *J. Ind. Eng. Chem.* **2015**, *22*, 317–323. https://doi.org/10.1016/j.jiec.2014.07.025.

(32) Wang, C. C.; Du, X. D.; Li, J.; Guo, X. X.; Wang, P.; Zhang, J. Photocatalytic Cr(VI) Reduction in Metal-Organic Frameworks: A Mini-Review. *Appl. Catal. B Environ.*

2016, *193*, 198–216. https://doi.org/10.1016/j.apcatb.2016.04.030.

(33) Fellahi, O.; Barras, A.; Pan, G. H.; Coffinier, Y.; Hadjersi, T.; Maamache, M.; Szunerits, S.; Boukherroub, R. Reduction of Cr(VI) to Cr(III) Using Silicon Nanowire Arrays under Visible Light Irradiation. *J. Hazard. Mater.* **2016**, *304*, 441–447. https://doi.org/10.1016/j.jhazmat.2015.11.020.

(34) Li, H. C.; Liu, W. J.; Han, H. X.; Yu, H. Q. Hydrophilic Swellable Metal-Organic Framework Encapsulated Pd Nanoparticles as an Efficient Catalyst for Cr(VI) Reduction. *J. Mater. Chem. A* **2016**, *4* (30), 11680–11687. https://doi.org/10.1039/c6ta03688k.

(35) Zhao, Y.; Zhao, D.; Chen, C.; Wang, X. Enhanced Photo-Reduction and Removal of Cr(VI) on Reduced Graphene Oxide Decorated with TiO2 Nanoparticles. *J. Colloid Interface Sci.* **2013**, *405*, 211–217. https://doi.org/10.1016/j.jcis.2013.05.004.

(36) Wei, H.; Hou, C.; Zhang, Y.; Nan, Z. Scalable Low Temperature in Air Solid Phase Synthesis of Porous Flower-like Hierarchical Nanostructure SnS2 with Superior Performance in the Adsorption and Photocatalytic Reduction of Aqueous Cr(VI). *Sep. Purif. Technol.* **2017**, *189* (August), 153–161. https://doi.org/10.1016/j.seppur.2017.08.014.

(37) Liu, L.; Luo, C.; Xiong, J.; Yang, Z.; Zhang, Y.; Cai, Y.; Gu, H. Reduced Graphene Oxide (RGO) Decorated TiO2microspheres for Visible-Light Photocatalytic Reduction of Cr(VI). *J. Alloys Compd.* **2017**, *690*, 771–776. https://doi.org/10.1016/j.jallcom.2016.08.197.

(38) Mitra, S.; Sarkar, A.; Sen, S. Removal of Chromium from Industrial Effluents Using Nanotechnology: A Review. *Nanotechnol. Environ. Eng.* **2017**, *2* (1), 1–14. https://doi.org/10.1007/s41204-017-0022-y.

(39) Wang, J.; Li, X.; Zhu, J.; Li, H.; Le, X. Mesoporous Yolk-Shell SnS2-TiO2 Visible Photocatalysts with Enhanced Activity and Durability in Cr(VI) Reduction. *Nanoscale* **2013**, *5* (5), 1876–1881. https://doi.org/10.1039/c2nr33755j.

(40) Dozzi, M. V.; Saccomanni, A.; Selli, E. Cr(VI) Photocatalytic Reduction: Effects of Simultaneous Organics Oxidation and of Gold Nanoparticles Photodeposition on TiO 2. *J. Hazard. Mater.* **2012**, *211–212*, 188–195. https://doi.org/10.1016/j.jhazmat.2011.09.038.

(41) Nasrallah, N.; Kebir, M.; Koudri, Z.; Trari, M. Photocatalytic Reduction of Cr(VI) on the Novel Hetero-System CuFe2O4/CdS. *J. Hazard. Mater.* **2011**, *185* (2–3), 1398–1404. https://doi.org/10.1016/j.jhazmat.2010.10.061.

(42) Zhang, L.; Niu, C. G.; Liang, C.; Wen, X. J.; Huang, D. W.; Guo, H.; Zhao, X. F.; Zeng, G. M. One-Step in Situ Synthesis of CdS/SnO2 Heterostructure with Excellent Photocatalytic Performance for Cr(VI) Reduction and Tetracycline Degradation. *Chem. Eng. J.* **2018**, *352* (May), 863–875. https://doi.org/10.1016/j.cej.2018.07.102.

(43) Fang, S.; Zhou, Y.; Zhou, M.; Li, Z.; Xu, S.; Yao, C. Facile Synthesis of Novel ZnFe2O4/CdS Nanorods Composites and Its Efficient Photocatalytic Reduction of Cr(VI) under Visible-Light Irradiation. *J. Ind. Eng. Chem.* **2018**, *58*, 64–73. https://doi.org/10.1016/j.jiec.2017.09.008.

(44) Xia, Q.; Huang, B.; Yuan, X.; Wang, H.; Wu, Z.; Jiang, L.; Xiong, T.; Zhang, J.; Zeng, G.; Wang, H. Modified Stannous Sulfide Nanoparticles with Metal-Organic Framework: Toward Efficient and Enhanced Photocatalytic Reduction of Chromium (VI) under Visible Light. *J. Colloid Interface Sci.* **2018**, *530*, 481–492. https://doi.org/10.1016/j.jcis.2018.05.015.

(45) Yuan, Y. J.; Chen, D. Q.; Shi, X. F.; Tu, J. R.; Hu, B.; Yang, L. X.; Yu, Z. T.; Zou, Z. G. Facile Fabrication of "Green" SnS2 Quantum Dots/Reduced Graphene Oxide Composites with Enhanced Photocatalytic Performance. *Chem. Eng. J.* **2017**, *313*, 1438–1446. https://doi.org/10.1016/j.cej.2016.11.049.

(46) Nezar, S.; Cherifi, Y.; Barras, A.; Addad, A.; Dogheche, E.; Saoula, N.; Laoufi, N. A.; Roussel, P.; Szunerits, S.; Boukherroub, R. Efficient Reduction of Cr(VI) under Visible Light Irradiation Using CuS Nanostructures. *Arab. J. Chem.* **2019**, *12* (2), 215–224. https://doi.org/10.1016/j.arabjc.2018.01.002.

(47) Velegraki, G.; Miao, J.; Drivas, C.; Liu, B.; Kennou, S.; Armatas, G. S. Fabrication of 3D Mesoporous Networks of Assembled CoO Nanoparticles for Efficient Photocatalytic Reduction of Aqueous Cr(VI). *Appl. Catal. B Environ.* **2018**, *221* (July 2017), 635–644. https://doi.org/10.1016/j.apcatb.2017.09.064.

(48) He, H.; Luo, Z.; Tang, Z. Y.; Yu, C. Controllable Construction of ZnWO4 Nanostructure with Enhanced Performance for Photosensitized Cr(VI) Reduction. *Appl. Surf. Sci.* **2019**, *490* (April), 460–468. https://doi.org/10.1016/j.apsusc.2019.05.260.

(49) Thwala, M. M.; Dlamini, L. N. Photocatalytic Reduction of Cr(VI) Using Mg-Doped WO3 Nanoparticles. *Environ. Technol. (United Kingdom)* **2019**, *3330* (Vi). https://doi.org/10.1080/09593330.2019.1629635.

(50) Duresa, L. W.; Kuo, D. H.; Ahmed, K. E.; Zeleke, M. A.; Abdullah, H. Highly Enhanced Photocatalytic Cr(vi) Reduction Using In-Doped Zn(O,S) Nanoparticles. *New J. Chem.* **2019**, *43* (22), 8746–8754. https://doi.org/10.1039/c9nj01511f.

(51) Wang, Y.; Su, Y.; Fang, W.; Zhang, Y.; Li, X.; Zhang, G.; Sun, W. SnO2/SnS2 Nanocomposite Anchored on Nitrogen-Doped RGO for Improved Photocatalytic Reduction of Aqueous Cr(VI). *Powder Technol.* **2020**, *363*, 337–348. https://doi.org/10.1016/j.powtec.2020.01.009.

(52) Wang, Y.; Wang, Q.; Zhan, X.; Wang, F.; Safdar, M.; He, J. Visible Light Driven Type II Heterostructures and Their Enhanced Photocatalysis Properties: A Review. *Nanoscale* **2013**, *5* (18), 8326–8339. https://doi.org/10.1039/c3nr01577g.

(53) Kabra, K.; Chaudhary, R.; Sawhney, R. L. Treatment of Hazardous Organic and Inorganic Compounds through Aqueous-Phase Photocatalysis: A Review. *Ind. Eng. Chem. Res.* **2004**, *43* (24), 7683–7696. https://doi.org/10.1021/ie0498551.

(54) Chaki, S. H.; Deshpande, M. P.; Trivedi, D. P.; Tailor, J. P.; Chaudhary, M. D.; Mahato, K. Wet Chemical Synthesis and Characterization of SnS2 Nanoparticles. *Appl. Nanosci.* **2013**, *3* (3), 189–195. https://doi.org/10.1007/s13204-012-0123-7.

(55) Damkale, S. R.; Arbuj, S. S.; Umarji, G. G.; Panmand, R. P.; Khore, S. K.; Sonawane, R. S.; Rane, S. B.; Kale, B. B. Two-Dimensional Hexagonal SnS2 Nanostructures for Photocatalytic Hydrogen Generation and Dye Degradation. *Sustain. Energy Fuels* **2019**, *3* (12), 3406–3414. https://doi.org/10.1039/c9se00235a.

(56) Zhang, Y. C.; Li, J.; Zhang, M.; Dionysiou, D. D. Size-Tunable Hydrothermal Synthesis of SnS 2 Nanocrystals with High Performance in Visible Light-Driven Photocatalytic Reduction of Aqueous Cr(VI). *Environ. Sci. Technol.* **2011**, *45* (21), 9324–9331. https://doi.org/10.1021/es202012b.

(57) Zhang, G.; Du, X.; Wang, Y.; Wang, H.; Wang, W.; Fu, Z. Controllable Synthesis of SnS2 Nanostructures with High Adsorption and Photocatalytic Activities. *Mater. Sci. Semicond. Process.* **2017**, *64* (February), 77–84. https://doi.org/10.1016/j.mssp.2017.03.010.

(58) Liu, H.; Su, Y.; Chen, P.; Wang, Y. Microwave-Assisted Solvothermal Synthesis of 3D Carnation-like SnS 2 Nanostructures with High Visible Light Photocatalytic Activity. *J. Mol. Catal. A Chem.* **2013**, *378*, 285–292. https://doi.org/10.1016/j.molcata.2013.06.021.

(59) Wang, S.; Yang, B.; Liu, Y. Synthesis of a Hierarchical SnS2 Nanostructure for Efficient Adsorption of Rhodamine B Dye. *J. Colloid Interface Sci.* **2017**, *507*, 225–233. https://doi.org/10.1016/j.jcis.2017.07.053.

(60) Derikvandi, H.; Nezamzadeh-Ejhieh, A. An Effective Wastewater Treatment Based on Sunlight Photodegradation by SnS2–ZnS/Clinoptilolite Composite. *Solid State Sci.* **2020**, *101* (January), 106127. https://doi.org/10.1016/j.solidstatesciences.2020.106127.

(61) Liu, S.; Yin, X.; Chen, L.; Li, Q.; Wang, T. Synthesis of Self-Assembled 3D Flowerlike SnS2 Nanostructures with Enhanced Lithium Ion Storage Property. *Solid State Sci.* **2010**, *12* (5), 712–718. https://doi.org/10.1016/j.solidstatesciences.2010.02.033.

(62) Zhou, X.; Zhou, T.; Hu, J.; Li, J. Controlled Strategy to Synthesize SnO2 Decorated

SnS2 Nanosheets with Enhanced Visible Light Photocatalytic Activity. *CrystEngComm* **2012**, *14* (17), 5627–5633. https://doi.org/10.1039/c2ce25309g.

(63) Fakhri, A.; Behrouz, S.; Pourmand, M. Synthesis, Photocatalytic and Antimicrobial Properties of SnO2, SnS2 and SnO2/SnS2 Nanostructure. *J. Photochem. Photobiol. B Biol.* **2015**, *149*, 45–50. https://doi.org/10.1016/j.jphotobiol.2015.05.017.

(64) Shi, W.; Huo, L.; Wang, H.; Zhang, H.; Yang, J.; Wei, P. Hydrothermal Growth and Gas Sensing Property of Flower-Shaped SnS 2 Nanostructures. *Nanotechnology* **2006**, *17* (12), 2918–2924. https://doi.org/10.1088/0957-4484/17/12/016.

(65) Xiong, Y.; Xu, W.; Ding, D.; Lu, W.; Zhu, L.; Zhu, Z.; Wang, Y.; Xue, Q. Ultra-Sensitive NH3 Sensor Based on Flower-Shaped SnS2 Nanostructures with Sub-Ppm Detection Ability. *J. Hazard. Mater.* **2018**, *341*, 159–167. https://doi.org/10.1016/j.jhazmat.2017.07.060.

(66) Zhong, H.; Yang, G.; Song, H.; Liao, Q.; Cui, H.; Shen, P.; Wang, C. X. Vertically Aligned Graphene-like SnS 2 Ultrathin Nanosheet Arrays: Excellent Energy Storage, Catalysis, Photoconduction, and Field-Emitting Performances. *J. Phys. Chem. C* **2012**, *116* (16), 9319–9326. https://doi.org/10.1021/jp301024d.

(67) Su, G.; Hadjiev, V. G.; Loya, P. E.; Zhang, J.; Lei, S.; Maharjan, S.; Dong, P.; M. Ajayan, P.; Lou, J.; Peng, H. Chemical Vapor Deposition of Thin Crystals of Layered Semiconductor Sns2 for Fast Photodetection Application. *Nano Lett.* **2015**, *15* (1), 506–513. https://doi.org/10.1021/nl503857r.

(68) Seo, J. W.; Jang, J. T.; Park, S. W.; Kim, C.; Park, B.; Cheon, J. Two-Dimensional SnS2 Nanoplates with Extraordinary High Discharge Capacity for Lithium Ion Batteries. *Adv. Mater.* **2008**, *20* (22), 4269–4273. https://doi.org/10.1002/adma.200703122.

(69) De, D.; Manongdo, J.; See, S.; Zhang, V.; Guloy, A.; Peng, H. High on/off Ratio Field Effect Transistors Based on Exfoliated Crystalline SnS2 Nano-Membranes. *Nanotechnology* **2013**, *24* (2). https://doi.org/10.1088/0957-4484/24/2/025202.

(70) Zhai, C.; Du, N.; Yang, H. Z. D. Large-Scale Synthesis of Ultrathin Hexagonal Tin Disulfide Nanosheets with Highly Reversible Lithium Storage. *Chem. Commun.* **2011**, *47* (4), 1270–1272. https://doi.org/10.1039/c0cc03023f.

(71) Mondal, C.; Ganguly, M.; Pal, J.; Roy, A.; Jana, J.; Pal, T. Morphology Controlled Synthesis of SnS2 Nanomaterial for Promoting Photocatalytic Reduction of Aqueous Cr(VI) under Visible Light. *Langmuir* **2014**, *30* (14), 4157–4164. https://doi.org/10.1021/la500509c.

(72) Kavitha, D.; Namasivayam, C. Experimental and Kinetic Studies on Methylene Blue Adsorption by Coir Pith Carbon. *Bioresour. Technol.* **2007**, *98* (1), 14–21. https://doi.org/10.1016/j.biortech.2005.12.008.

(73) Hema, M.; Arivoli, S. Rhodamine B Adsorption by Activated Carbon: Kinetic and Equilibrium Studies. *Indian J. Chem. Technol.* **2009**, *16* (1), 38–45.

(74) Bian, X.; Lu, X.; Xue, Y.; Zhang, C.; Kong, L.; Wang, C. A Facile One-Pot Hydrothermal Method to Produce SnS2/Reduced Graphene Oxide with Flake-on-Sheet Structures and Their Application in the Removal of Dyes from Aqueous Solution. *J. Colloid Interface Sci.* **2013**, *406*, 37–43. https://doi.org/10.1016/j.jcis.2013.05.075.

(75) Peng, L.; Qin, P.; Lei, M.; Zeng, Q.; Song, H.; Yang, J.; Shao, J.; Liao, B.; Gu, J. Modifying Fe3O4 Nanoparticles with Humic Acid for Removal of Rhodamine B in Water. *J. Hazard. Mater.* **2012**, *209–210*, 193–198. https://doi.org/10.1016/j.jhazmat.2012.01.011.

(76) Qin, Y.; Long, M.; Tan, B.; Zhou, B. RhB Adsorption Performance of Magnetic Adsorbent Fe3O4/RGO Composite and Its Regeneration through A Fenton-like Reaction. *Nano-Micro Lett.* **2014**, *6* (2), 125–135. https://doi.org/10.1007/BF03353776.

(77) Bhatnagar, A.; Jain, A. K. A Comparative Adsorption Study with Different Industrial Wastes as Adsorbents for the Removal of Cationic Dyes from Water. *J. Colloid Interface Sci.* **2005**, *281* (1), 49–55. https://doi.org/10.1016/j.jcis.2004.08.076.

(78) Anandkumar, J.; Mandal, B. Adsorption of Chromium(VI) and Rhodamine B by Surface Modified Tannery Waste: Kinetic, Mechanistic and Thermodynamic Studies. *J. Hazard. Mater.* **2011**, *186* (2–3), 1088–1096. https://doi.org/10.1016/j.jhazmat.2010.11.104.

(79) Liu, X.; Tian, J.; Li, Y.; Sun, N.; Mi, S.; Xie, Y.; Chen, Z. Enhanced Dyes Adsorption from Wastewater via Fe3O4 Nanoparticles Functionalized Activated Carbon. *J. Hazard. Mater.* **2019**, *373* (December 2018), 397–407. https://doi.org/10.1016/j.jhazmat.2019.03.103.

(80) Selvam, P. P.; Preethi, S.; Basakaralingam, P.; N.Thinakaran; Sivasamy, A.; Sivanesan, S. Removal of Rhodamine B from Aqueous Solution by Adsorption onto Sodium Montmorillonite. *J. Hazard. Mater.* **2008**, *155* (1–2), 39–44. https://doi.org/10.1016/j.jhazmat.2007.11.025.

(81) Zhang, Z.; Kong, J. Novel Magnetic Fe3O4@C Nanoparticles as Adsorbents for Removal of Organic Dyes from Aqueous Solution. *J. Hazard. Mater.* **2011**, *193*, 325–329. https://doi.org/10.1016/j.jhazmat.2011.07.033.

(82) Zhang, Z. yang; Xu, X. cheng. Wrapping Carbon Nanotubes with Poly (Sodium 4-Styrenesulfonate) for Enhanced Adsorption of Methylene Blue and Its Mechanism. *Chem. Eng. J.* **2014**, *256*, 85–92. https://doi.org/10.1016/j.cej.2014.06.020.

(83) Wang, Q.; Ju, J.; Tan, Y.; Hao, L.; Ma, Y.; Wu, Y.; Zhang, H.; Xia, Y.; Sui, K. Controlled Synthesis of Sodium Alginate Electrospun Nanofiber Membranes for Multi-Occasion Adsorption and Separation of Methylene Blue. *Carbohydr. Polym.* **2019**, *205* (October 2018), 125–134. https://doi.org/10.1016/j.carbpol.2018.10.023.

(84) Asfaram, A.; Ghaedi, M.; Hajati, S.; Goudarzi, A.; Bazrafshan, A. A. Simultaneous Ultrasound-Assisted Ternary Adsorption of Dyes onto Copper-Doped Zinc Sulfide Nanoparticles Loaded on Activated Carbon: Optimization by Response Surface Methodology. *Spectrochim. Acta - Part A Mol. Biomol. Spectrosc.* **2015**, *145*, 203–212. https://doi.org/10.1016/j.saa.2015.03.006.

(85) Wang, N.; Chen, J.; Wang, J.; Feng, J.; Yan, W. Removal of Methylene Blue by

Polyaniline/TiO 2 Hydrate: Adsorption Kinetic, Isotherm and Mechanism Studies. *Powder Technol.* **2019**, *347*, 93–102. https://doi.org/10.1016/j.powtec.2019.02.049.

(86) Egbosiuba, T. C.; Abdulkareem, A. S.; Kovo, A. S.; Afolabi, E. A.; Tijani, J. O.; Auta, M.; Roos, W. D. Ultrasonic Enhanced Adsorption of Methylene Blue onto the Optimized Surface Area of Activated Carbon: Adsorption Isotherm, Kinetics and Thermodynamics. *Chem. Eng. Res. Des.* **2020**, *153*, 315–336. https://doi.org/10.1016/j.cherd.2019.10.016.

(87) Shaban, Y. A. Effective Photocatalytic Reduction of Cr(VI) by Carbon Modified (CM)-n-TiO2 Nanoparticles under Solar Irradiation. *World J. Nano Sci. Eng.* **2013**, *03* (04), 154–160. https://doi.org/10.4236/wjnse.2013.34018.

(88) Qu, J.; Chen, D.; Li, N.; Xu, Q.; Li, H.; He, J.; Lu, J. Coral-Inspired Nanoscale Design of Porous SnS2 for Photocatalytic Reduction and Removal of Aqueous Cr (VI). *Appl. Catal. B Environ.* **2017**, *207*, 404–411. https://doi.org/10.1016/j.apcatb.2017.02.050.

(89) Mansingh, S.; Padhi, D. K.; Parida, K. M. Enhanced Visible Light Harnessing and Oxygen Vacancy Promoted N, S Co-Doped CeO2 Nanoparticle: A Challenging Photocatalyst for Cr(vi) Reduction. *Catal. Sci. Technol.* **2017**, *7* (13), 2772–2781. https://doi.org/10.1039/c7cy00499k.

(90) Faisal, M.; Harraz, F. A.; Al-Salami, A. E.; El-Toni, A. M.; Almadiy, A. A.; Khan, A.; Labis, J. P.; Al-Sayari, S. A.; Al-Assiri, M. S. Enhanced Photocatalytic Reduction of Cr(VI) on Silver Nanoparticles Modified Mesoporous Silicon under Visible Light. *J. Am. Ceram. Soc.* **2019**, *102* (9), 5071–5081. https://doi.org/10.1111/jace.16400.

(91) Park, S.; Selvaraj, R.; Meetani, M. A.; Kim, Y. Journal of Industrial and Engineering Chemistry Enhancement of Visible-Light-Driven Photocatalytic Reduction of Aqueous Cr (VI) with Fl Ower-like In3 + -Doped SnS 2. *J. Ind. Eng. Chem.* **2017**, *45*, 206–214. https://doi.org/10.1016/j.jiec.2016.09.024.

(92) Mu, R.; Xu, Z.; Li, L.; Shao, Y.; Wan, H.; Zheng, S. On the Photocatalytic Properties of Elongated TiO2 Nanoparticles for Phenol Degradation and Cr(VI) Reduction. *J. Hazard. Mater.* **2010**, *176* (1–3), 495–502.

https://doi.org/10.1016/j.jhazmat.2009.11.057.

(93) Li, J.; Peng, T.; Zhang, Y.; Zhou, C.; Zhu, A. Polyaniline Modified SnO2 Nanoparticles for Efficient Photocatalytic Reduction of Aqueous Cr(VI) under Visible Light. *Sep. Purif. Technol.* **2018**, *201* (December 2017), 120–129. https://doi.org/10.1016/j.seppur.2018.03.010.

(94) Xu, Y.; Wang, D.; Xie, M.; Jing, L.; Huang, Y.; Huang, L.; Xu, H.; Li, H.; Xie, J. Novel Broad Spectrum Light Responsive PPy/Hexagonal-SnS2 Photocatalyst for Efficient Photoreduction of Cr(VI). *Mater. Res. Bull.* **2019**, *112* (December 2018), 226–235. https://doi.org/10.1016/j.materresbull.2018.12.017.